Advancing liquid crystal elastomers through copolymerization, nanostructures, and templated amorphous polymers

Dissertation

Presented in Partial Fulfillment of the Requirements for the Degree Doctor of Philosophy
in the Graduate School of The Ohio State University

By

Robert Lewis Dupont, M.S.

Graduate Program in Chemical Engineering

The Ohio State University

2024

Dissertation Committee

Xiaoguang "William" Wang, Advisor

Stuart Cooper

Lisa M. Hall

Abstract

Shape memory polymers (SMPs) have seen increased use in soft robotics, actuators, drug delivery, and optics because of their ability to respond to external stimuli in a variety of ways. As a representative class of shape memory polymers, liquid crystal elastomers (LCEs) have seen expanded interest in recent years, owing to their unique ability to reversibly deform to stimuli without the need for outside deformations. LCEs rely on liquid crystals (LCs), which are self-aligning, rod-like molecules that exhibit a phase between solids and liquids, for their unique reversibility. There is an opportunity to increase the usefulness of LCEs through copolymerization and the addition of nanostructures on the surface. In addition, traditional LCEs are hampered in some applications, namely biomedical applications, because of the inherent danger many of them pose to cells. This work seeks to improve LCEs in three main ways: copolymerizing LC monomers, creating nanoscopic surface structures, and templating the LC order into non-LC monomers. By copolymerizing different LC monomers together, we were able to provide a new avenue to control the magnitude and direction of LCE deformations. With the addition of densely packed, nanoscopic surface structures, we enhanced the adhesive force of LCE films increasing their utility in soft robotics. Finally, by templating the order of LCs to non-LC monomers, we created LCE-like materials that exhibit kinetically trapped, reversible deformations with polymers that are better suited for biomedical applications. These three

thrusts have expanded the design space for LCEs and have introduced new materials and physical properties.

Dedication

I dedicate this work to my parents, my community here at The Ohio State University, and to God. Without any of them, I would not be able to write this document.

Acknowledgments

I would like to acknowledge my adviser for his constant passion and love of science that kept me going through the degree. I would like to acknowledge Dr. Yang Xu for his guidance and work on many of these projects. His help during his Postdoc was invaluable. I would also like to acknowledge my colleague and friend Ufuoma Kara for his constant support and help devising new strategies in the lab. I would like to acknowledge Fatemeh Azadi for the breath of fresh air that she brought to many of these projects. Without her help, these projects may never have seen completion. Finally, I would like to acknowledge Dr. Mike McConney and his lab at the Air Force Research Lab for their help putting the finishing touches on a couple of these thrusts.

Vita

2021……………….…………….M.S. Chemical Engineering, The Ohio State University

2021 to present …………………..Graduate Teaching Assistant, Department of Chemical and Biomolecular Engineering, The Ohio State University

2024………………………………CBE Outstanding Graduate Researcher Award, The Ohio State University

Publications

Lv, H.; Yao, Y.; Yuan, M.; Chen, G.; Wang, Y.; Rao, L.; Li, S.; Kara, U. I.; **Dupont, R. L.**; Zhang, C.; Chen, B.; Liu, B.; Zhou, X.; Wu, R.; Adera, S.; Che, R.; Zhang, X.; Wang, X. Functional Nanoporous Graphene Superlattice. Nature Communications, 2024, 15, 1295.

Zhang, W.; Wang, R.; Liu, M.; Li, S.; Vokoun, A. E.; Deng, W.; **Dupont, R. L.**; Zhang, F.; Li, S.; Wang, Y.; Liu, Z.; Zheng, Y.; Liu, S.; Yang, Y.; Wang, C.; Yu, L.; Yao, Y.; Wang, X.; Wang, C. Single-Molecule Visualization Determines Conformational Sub-State Ensembles in β-Sheet-Rich Peptide Fibrils. Science Advances, 2023, 9, adg7943.

Lv, H.; Yao, Y.; Li, S.; Wu, G.; Zhao, B.; Zhou, X.; **Dupont, R. L.**; Kara, U. I.; Zhou, Y.; Xi, S.; Liu, B.; Che, R.; Zhang, J.; Xu, H.; Adera, S.; Wu, R.; Wang, X. Staggered Circular Nanoporous Graphene Converts Electromagnetic Waves into Electricity. Nature Communications, 2023, 14, 1982.

Zhang, M.; Vokoun, A. E.; Chen, B.; Deng, W.; **Dupont, R. L.**; Xu, Y.; Wang, X. Advancements in Droplet Reactor Systems Represent New Opportunities in Chemical Reactor Engineering: A Perspective. The Canadian Journal of Chemical Engineering, 2023, 101, 5189-5207.

Dhar, M.; Kara, U. I.; Das, S.; Xu, Y.; Mandal, S.; **Dupont, R. L.**; Boerner, E. C.; Chen, B.; Yao, Y.; Wang, X.; Manna, U. Design of a Self-Cleanable Multilevel Anticounterfeiting Interface Through Covalent Chemical Modulation. Materials Horizons, 2023, 10, 2204-2214.

Xu, Y.; Yao, Y.; Deng, W.; Fang, J.-C.; **Dupont, R. L.**; Zhang, M.; Copar, S.; Tkalec, U.; Wang, X. Magnetocontrollable Droplet Mobility on Liquid Crystal-Infused Porous Surfaces. Nano Research, 2023, 16, 5098-5107.

Xu, Y.; Chang, Y.; Yao, Y.; Zhang, M.; **Dupont, R. L.**; Rather, A. M.; Bao, X.; Wang, X. Modularizable Liquid Crystal-Based Open Surfaces Enable Programmable Chemical Transport and Feeding Using Liquid Droplets. Advanced Materials, 2022, 34, 2108788.

Rather, A. M.; Xu, Y.; Chang, Y.; **Dupont, R. L.**; Borbora, A.; Kara, U. I.; Fang, J.-C.; Mamtani, R.; Zhang, M.; Yao, Y.; Adera, S.; Bao, X.; Manna, U.; Wang, X. Stimuli-Responsive Liquid Crystal-Infused Porous Surfaces for Manipulation of Underwater Gas Bubble Transport and Adhesion. Advanced Materials, 2022, 2110085.

Borbora, A.; **Dupont, R. L.**; Yang, X.; Wang, X.; Manna, U. Dually Reactive Multilayer Coatings Enable Orthogonal Manipulation of Underwater Superoleophobicity and Oil Adhesion via Post-Functionalization. Materials Horizons, 2022, 9, 991-1001.

Zhang, W.; Liu, M.; **Dupont, R. L.**; Huang, K.; Yu, L.: Liu, S.; Wang, X.; Wang, C. Conservation and Identity Selection of Cationic Residues Flanking the Hydrophobic Regions in Intermediate Filament Superfamily. Frontiers in Chemistry, 2021, 9, 752630.

Xu, Y.*; **Dupont, R. L.***; Yao, Y.*; Zhang, M.; Fang, J.-C.; Wang, X. Random Liquid Crystalline Copolymers Consisting of Prolate and Oblate Liquid Crystal Monomers. Macromolecules, 2021, 54, 5376-5387.

Yu, L.; Zhang, W.; Luo, W.; **Dupont, R. L.**; Xu, Y.; Wang, Y.; Tu, B.; Xu, H.; Wang, X.; Fang, Q.; Yang, Y.; Wang, C.; Wang, C. Molecular Recognition of Human Islet Amyloid Polypeptide Assembly by Selective Oligomerization of Thioflavin-T. Science Advances, 2020, 6, eabc1449.

Xu, Y.; Rather, A. M.; Song, S.; Fang, J.-C.; **Dupont, R. L.**; Kara, U. I.; Chang, Y.; Paulson, J. A.; Qin, R.; Bao, X.; Wang, X. Ultrasensitive and Selective Detection of SARS-CoV-2 using Thermotropic Liquid Crystals and Image-based Machine Learning. Cell Reports Physical Science, 2020, 1, 100276.

Rather, A. M.; Xu, Y.; **Dupont, R. L.**; Wang, X. Polymeric Membranes in Wastewater Treatment. Book Title: Nanoscale Engineering of Biomaterials: Properties and Applications. Editors: Pandey, L.; Hasan, A. Springer Nature. 2022, 487-515.

*indicates co-first authored publications

Fields of Study

Major Field: Chemical Engineering

Table of Contents

List of Tables

List of Figures

Chapter 1 Introduction

1.1 Polymers and Crystallinity

Polymers, a ubiquitous part of everyday life, are macromolecules composed of thousands of individual units, namely monomers. They can be composed of a single type of monomer, creating a homopolymer, or multiple monomers, creating a copolymer. The monomers react together to form new covalent bonds creating a polymer backbone. This can be done through a variety of chemistries, with the two most common being radical and condensation polymerization. Radical polymerization relies on the breaking of double bonds to create free radical electrons that attack a neighboring monomer. This creates a new carbon-carbon bond. On the other hand, condensation polymerization forms new bonds between carbon and either nitrogen or oxygen, splitting off a water molecule. This is accomplished through the combination of carboxylic acid groups and commonly either alcohol or amine groups. One of the most common types of materials made this way are nylons.

Because of their unique structure, polymers exhibit useful and interesting properties. Specifically, entanglements between polymer chains occur that allows them to form flexible and elastic solids. These polymer chains statistically and thermodynamically prefer to conform into a random coil shape, where they ball up into a jumble like a bowl of spaghetti. The entanglements, random coil conformations, and the restrictions from the covalent bonds making up the backbone prevent the polymer chains from fully crystallizing. Instead, they tend to form amorphous structures that lack long-range order.

However, in some cases, the polymer chains are able to form regions of crystallinity, where the chains align together. This is most common when the polymer chains have structural components in either the chain or the side groups that allows them to strongly interact. For instance, because of the polyamide bonds in nylon, the polymer chains are polar and are also able to form hydrogen bonds. The semi-crystallinity of these materials gives them an increased strength and rigidity. However, fully crystallizing polymer chains is extremely difficult because of their random and jumbled nature. In other cases, such as in liquid crystalline or conjugated polymers, the rigidity and highly polar nature of the molecules allows them to strongly align. Examples of conjugated monomers can be found in Figure 1.[1] Conjugated polymers also tend to be highly conductive, making them a great choice for solar panels and electronics.[1-6]

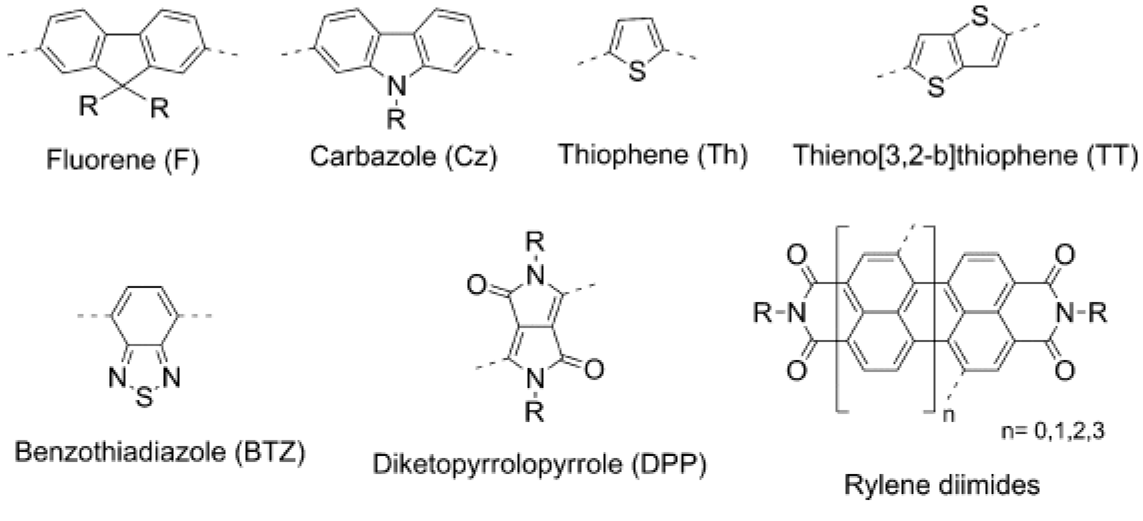

Figure 1. Molecular formulas of common conjugated monomers.[1]

Similarly, liquid crystals (LCs) are molecules that exhibit a phase between the solid and liquid phase, namely the LC phase. In this phase, the LCs retain some of the long-range order of solids while also being able to flow like liquids. This is because of their unique structure, where a rigid core is augmented with polar groups and flexible sections, as seen in Figure 2. When in the LC phase, the most common being the nematic phase, the LC molecules self-align into a unified direction. In some cases, they are even able to align spatially, forming rows and columns, such as in the smectic phase. The LC phase can be controlled through changes in concentration, such as for lyotropic LCs, or through changes in temperature, such as for thermotropic LCs. Other methods can be used to control the alignment of the LCs and their phase including the addition of non-LC molecules, the conformational switching of azobenzene-derived molecules in response to ultraviolet light, and external magnetic fields.

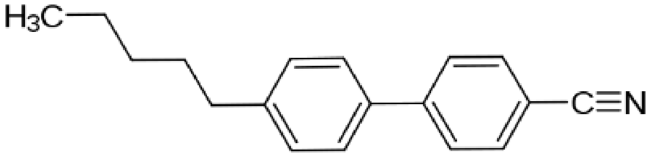

Figure 2. Molecular formula of 4-cyano-4'-pentylbiphenyl (5CB), a representative liquid crystal molecule.

1.2 Shape Memory Polymers, Hydrogels, and Dielectric Elastomers

Responsive polymeric materials have seen extended use in areas that require controlled shape deformations, such as drug delivery[7-9] and soft robotics.[10-12] These materials can take the shape of sol-gels, where polymer networks are swollen by a solvent (commonly water), or solid polymer networks, like shape memory polymers and dielectric elastomers. With sol-gels, the material changes its shape in response to the addition or removal of a solvent, whereupon it swells into a hydrated state or shrinks into a dehydrated state, respectively.[13] When controlled, this allows the material to apply an external force which has found practical use in soft robotics.[14,15] In some cases, these sol-gel transitions can be caused by other external stimuli, such as heat.[16] However, these deformations are usually the same in all directions.

In contrast to this, shape memory polymers and dielectric elastomers exhibit anisotropic deformations. Shape memory polymers rely on conformational changes between a kinetically trapped, temporary shape and a thermodynamically favored, memorized shape. Shape memory polymers are a type of material that exhibit a macroscopic deformation in response to an external stimulus, usually a temperature change. By heating these materials, manually deforming them, and then cooling them back down, a temporary shape can be created and retained. The original, memorized shape can be returned to upon heating again beyond the original temperature. The increase in temperature allows the internal stresses to pull the material back into its original shape alleviating the built-up stress. See Figure 3 for an example.[17] There has been a large body of work related to shape memory polymers to increase their shape memory properties, including the addition of other polymers and nanofillers to create nanocomposites.[18] At the same time, researchers have been working to create double- and triple- shape memory polymers that exhibit multiple shape deformations and temporary shapes, though they still require outside influence to create the temporary shape.[19-21] Similarly, dielectric elastomers exhibit unidirectional deformations in response to a voltage across their thickness, though they often require reswelling after deforming.[22-25]

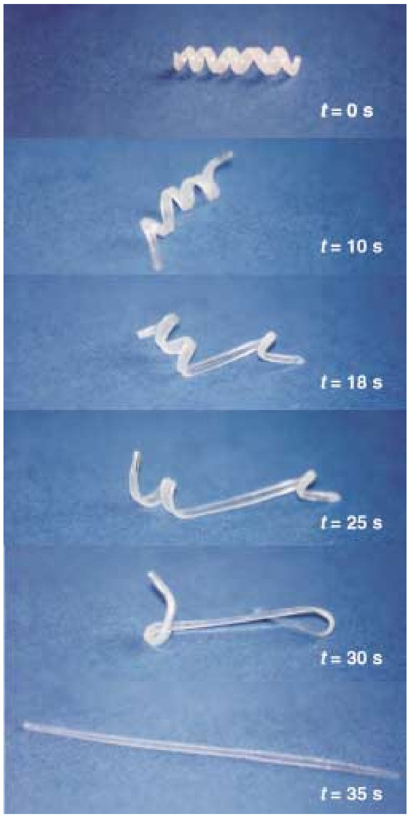

Figure 3. Example of a shape memory polymer returning to its original shape from Lendlein et al.[17]

1.3 Liquid Crystal Elastomers

As a unique form of shape memory polymers, liquid crystal elastomers (LCEs) have seen an incredible growth in research articles over the years.[26,27] This is because of their ability to deform reversibly in response to an external stimulus, which separates them from other types of shape memory polymers. By utilizing the self-ordering of LC moieties along the backbone of the polymer chains, either within the backbone or attached to the side as side groups, the polymer chains can be made to switch between an elongated chain conformation and the thermodynamically favored random coil conformation. When lightly crosslinked together, this switch between chain conformations causes a macroscopic material deformation, exemplified by the complex deformations found in Figure 4.[28] This only works when the polymer chain is created within an aligned LC system. The direction of deformation can be controlled through tuning the alignment of the LCs. For instance, if the alignment on one surface is rotated by 90 degrees from the other surface, a twisting deformation can be created. Likewise, if the LCs are aligned parallel to one surface but perpendicular to the other, then the material will curl, as one side expands and the other contracts.

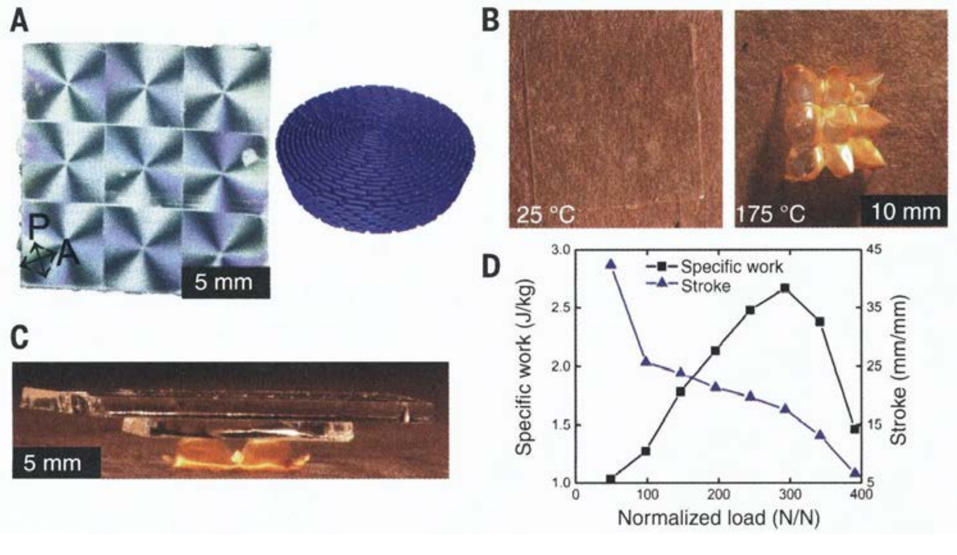

Figure 4. Complex shape deformations created through photoaligning by Ware et al.[28]

Generally, liquid crystal monomers come in two broad forms, main-chain, where the LCs make up part of the polymer backbone, and side-chain, where the LCs are attached to the backbone by short, flexible carbon chains. The research contained within this document is mainly based on side-chain LCEs. Side-chain LCEs come in two main forms, those being end-on, where the LC moiety is attached on its the end, and side-on, where the LC moiety is attached on its side. Their attachment to the backbone causes the end-on moieties to align perpendicularly to the polymer backbone while the side-on moieties align parallelly to the backbone. When comparing the two, the polymer materials will deform in opposite directions with respect to the LC director, which is the average direction of the long axis of the LC moieties. Generally, end-on-based LCEs will extend in the direction of the director and side-on-based LCEs will contract in the direction of the director. This opens up opportunities for the intelligent design of LCEs.

1.4 Opportunities, Challenges, and Motivation

A main focus of LCE research has been in the area of soft robotics.[29-31] This includes the use of complicated photoalignment methods[28] and 3D printing advancements.[32-34] To add to this, the first thrust of my research focused on the effect of the random copolymerization of different kinds of LC monomers. Most research has only used one type of LC monomer and has neglected to investigate the use of multiple types. We discovered that using both types of side chain monomers allows for a more direct control over the direction and magnitude of the stimuli-responsive deformation of LCEs. This also enables the easy patterning of different directions and magnitudes of deformations utilizing simple alignment methods. More importantly, this knowledge can easily be included in existing 3D printing technologies and photoalignment methods to enable even more complex shape deformations.

The second thrust of my research focused on unlocking a new utility for LCEs by investigating the creation of nanoscale structures on their surface. This takes inspiration from nature, specifically the structures on the footpads of geckos.[35,36] These structures increase the surface contact area and adhesion forces of the geckos and allows them to crawl over all sorts of surfaces and geometries. By using a template to create nanoscopic surface structures, we were able to enhance the adhesion of LCE films while maintaining their unique shape deformations. In fact, the two can be synergistically combined to enable new applications for soft robotics.

The final thrust of my research includes efforts to circumvent the challenges common with LCEs, that being the complex synthesis required for their monomers, their relative cost, and their inability to be used in many bio-based applications. The molecular structure of LCs is both what provides them with their unique stimuli-responsive deformations and what hinders their use in some applications. This also means that cheaper, commodity polymers, such as poly(methyl methacrylate) and polystyrene which lack the proper structural motifs, are intrinsically unable to create materials that exhibit macroscopic deformations. However, we discovered that the intrinsic ordering of a nematic LC solvent could be imprinted into these intrinsically amorphous polymer chains creating stretched and aligned chains. These can then be crosslinked which allows them to deform similarly to conventional LCEs. This expands LCE-like materials into new areas and enables their use in bio-based applications.

Chapter 2 Random liquid crystalline copolymers consisting of prolate and oblate liquid crystal monomers

2.1 Preface

This chapter is adapted from a published paper titled “Random Liquid Crystalline Copolymers Consisting of Prolate and Oblate Liquid Crystal Monomers” published in *Macromolecules* on June 7th, 2021. It is focused on the first main thrust of my work copolymerizing different liquid crystal monomers together to control the magnitude and direction of the temperature-dependent macroscopic deformations.

2.2 Abstract

Interactions between side chains of polymers have been utilized to tune the thermal and mechanical properties of polymeric materials. In liquid crystal elastomers (LCE), previous studies have demonstrated that the configuration of liquid crystal (LC) monomers, specifically oblate or prolate, determines the direction of macroscopic material deformations relative to the orientational ordering of the LC functional groups. However, the effects of the copolymerization between different configurations of LC monomers on the phase behaviors and thermomechanical properties of LCEs have not been explored. Here, we reveal that statistically random copolymers of LC monomers with different configurations destabilize the orientational order of the LC functional groups, whereas random insertion of LC monomers with the same configuration preserves the packing of the constituent mesogenic functional groups. We further demonstrate how this fundamental

understanding can be applied to control both the direction and magnitude of the thermally triggered mechanical deformations of LC copolymer networks.

2.3 Introduction

Soft polymeric materials with complex shape transformations in response to environmental cues have shown great potential in applications ranging from drug delivery[37,38] to soft robotics.[19-23,39-50] A variety of polymeric materials, including hydrogels, shape memory polymers, and dielectric elastomers, have been reported to exhibit stimuli-responsive shape deformations. Thermally responsive hydrogels, such as poly(N-isopropylacrylamide), consist of a three-dimensional network of lightly crosslinked polymer chains that can reversibly change their shape between a swollen hydrated state and a shrunken dehydrated state.[51-57] The intrinsic mechanical properties of stimuli-responsive hydrogels, however, are typically the same in all directions, leading to isotropic deformations. Another group of shape changing materials, called shape memory polymers, can maintain temporary shapes with kinetically trapped polymer states with low conformational entropy and can return to their original shape when triggered by an external stimulus.[19,20,39,46,58] Although recent technological advances have observed the development of double- and triple-shape memory polymers, the fact that these materials can only return from a deformed state to the original, memorized state and are not able to deform out of the memorized state means that shape memory polymers do not allow for predetermined and reversible shape deformations. Dielectric elastomers, another well-known class of shape changing polymers, show deformations caused by Coulombic forces, with a contraction parallel and an expansion perpendicular to the electric field direction.[22-

[24,59,60] However, their reliance on a directional and high voltage makes non-uniform deformations on the microscale challenging.

Liquid crystal elastomers (LCEs) capitalize on the interplay between the self-association of liquid crystal (LC) functional groups and the entropic conformation of polymer backbones, resulting in phase-dependent macroscopic shape deformations.[32,61-66] Past studies have shown that LCEs are capable of exhibiting a rich palette of reversible and well-programmed anisotropic shape changes in response to a wide range of external stimuli, including heat,[67,68] solvents,[69] light,[33,70-73] and magnetic[31,74] and electric fields,[75] and have attracted great interest for their potential in the design and synthesis of responsive biomedical devices,[76-81] soft actuators and robotics,[29,34,82-97] and active surface structures.[28,30,98-107] LC moieties can be incorporated into polymer chains as either part of the polymer backbone (main-chain LCE) or the pendant functional group (side-chain LCE). Previous studies have shown that in LC phases, the conformation of LC polymer chains can deviate from statistically spherical random coils, depending on the configuration of the pendant LC functional groups, as seen in Figure 5.[27,62,63] For prolate LC polymers, polymer backbones align along the orientation of the mesogenic groups (called the director), resulting in a longer radius of gyration parallel to the LC director ($R_{\parallel}$) than that perpendicular to the LC director ($R_{\perp}$), seen in Figure 5A. This anisotropy gives rise to a uniaxial contraction of the respective LCE parallel to the LC director above the LC–isotropic phase transition temperatures ($T_{\text{LC–I}}$). In contrast, for oblate LC polymers in LC phases, the radius of gyration parallel to the director is shorter than the radius perpendicular, that is $R_{\parallel} < R_{\perp}$ (Figure 5B), which results in a uniaxial elongation of the

LCE parallel to the director above the $T_{\mathrm{LC-I}}$. Though the polymer chain conformation and the consequent shape deformations of LCEs made purely of one configuration of LC monomer, either prolate or oblate, have been extensively studied, to the best of our knowledge, the effect of the copolymerization of LC monomers with different configurations on the polymer conformation and the consequent LCE shape deformation remains hidden.

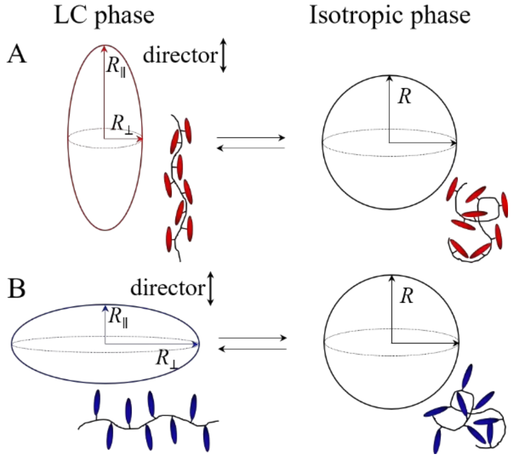

Figure 5. Polymer chain conformation and consequent mechanical deformation of LC polymers made of (A) prolate LCs and (B) oblate LCs.

In this chapter, we report the synthesis of random LC copolymers consisting of a combination of prolate and oblate reactive LC monomers. We demonstrate that the orientational order of LC functional groups is destabilized in random LC copolymers consisting of both prolate and oblate monomers, whereas a random insertion of the same configuration of LC monomers, e.g., oblate monomers, preserves the packing of the LC pendant groups on the polymer backbone. Furthermore, we illustrate the control over both the direction and magnitude of thermally triggered shape deformations of random LC copolymers by tuning LC monomer configurations and chemical compositions. Overall, our results not only provide insight into how LC monomer configurations and the chemical composition of random LC copolymers affect the thermal and mechanical properties of the formed LCE through the coupling of LC pendant groups, but also demonstrate a new design principle to program deformation behaviors of LCE structures by patterning local LC monomer configurations.

2.4 Experimental Section

2.4.1 Materials

Oblate liquid crystal (LC) monomers 4-(6-acryloxy-hex-1-yl-oxy) phenyl 4-(hexyloxy) benzoate (LCM1) and 4-methoxybenzoic acid 4-(6-acryloyloxyhexyloxy) phenyl ester (LCM2) were purchased from Synthon Chemicals GmbH & Co., Germany, and used as received. Prolate LC monomer 4’’-acryloyloxybutyl 2,5-di(4’-butyloxybenzoyloxy) benzoate (LCM3) was synthesized following the route described in a previous study.[85] Non-mesogenic crosslinker 1,6-hexanediol diacrylate (HDDA), photoinitiator 2-hydroxy-2-methylpropiophenone (DMPAP), reversible addition-fragmentation chain transfer (RAFT) agent 2-(dodecylthiocarbonothioylthio)-2-methylpropionic acid, poly(pyromellitic dianhydride-co-4,4′-oxydianiline) amic acid (PAA), 1-methyl-2-pyrrolidinone, and anhydrous dichloromethane were obtained from Sigma-Aldrich. Sylgard 184 silicone kit for the synthesis of polydimethylsiloxane (PDMS) was purchased from Ellsworth Adhesive Systems. All chemicals and reagents were used as received without further purification. Magnets were obtained from K&J Magnetics, Inc. Polyimide

(PI 2556) was purchased from HD Microsystems. Si wafers were purchased from UniversityWafer, Inc.

2.4.2 Synthesis of Random LC Copolymer for Phase Behavior Measurement

To synthesize random LC copolymers, we first dissolved LC monomers in dichloromethane at 10% by weight. DMPAP was then added as a photoinitiator at 2% by weight based on the weight of LC monomers. The mixture was photopolymerized for 40 minutes using a UV lamp that delivers 10 mW/cm2. Subsequently, dichloromethane was evaporated, and the formed polymers were collected for further characterizations. In the RAFT-mediated synthesis of random copolymers, RAFT agent 2-(dodecylthiocarbonothioylthio)-2-methylpropionic acid was added to the LC monomer dichloromethane solution with the molar ratio of [RAFT]:[photoinitiator]:[monomer] = 1:1:50, followed by solvent evaporation and photopolymerization described before.

2.4.3 Thermal Characterization

Phase transition temperatures of LC monomer mixtures and their respective LC polymers were characterized by differential scanning calorimetry (DSC) using a TA DSC Q100 Instrument. Heating and cooling rates in the DSC measurements were 2 °C/minute.

2.4.4 Preparation of Polyimide-Coated Glass Slides

A Laurell Technologies WS-650Mz-23NPPB spin processor was utilized to spin-coat a mixture of PAA, at 10% by volume, and 1-methyl-2-pyrrolidinone, at 90% by volume, on a cleaned glass slide at 4,000 rpm for 2 minutes. The coated glass slides were then heated at 350 °C for 3 hours to polymerize the polyimide and finish the coating process.

Finally, we used a velvet cloth to rub the surface of the polyimide unidirectionally 90 times to impart a directional alignment templated for the LC mixtures.

2.4.5 Fabrication of Optical Cells

Optical cells were prepared by pairing two polyimide-coated glass slides together with 50 μm spacers. For the top and bottom glass slides, we set the polyimide's alignment to be parallel to each other.

2.4.6 Microfabrication of PDMS Molds

We first fabricated designed microplates on Si wafers through photolithography and reactive ion etching. The photoresist patterning was created using UV exposure from a Heidelberg MLA150 Maskless Aligner, which acted as a mask for the anisotropic etching of Si wafers by using an STS ICP RIE System. After fabrication, the photoresist was removed by oxygen plasma. PDMS molds for LCE microplate fabrication were then prepared through the polymerization of well mixed PDMS precursors on top of the surface-attached microstructures on the Si wafers.

2.4.7 LCE Shape Deformation Characterization

Mixtures containing LC monomers, photoinitiator DMPAP, and crosslinker HDDA were prepared by using dichloromethane as a solvent. After mixing, the dichloromethane was evaporated. Either LCE films or LCE microplates were synthesized for the quantification of shape deformations as a function of temperature. The LCE sheets were synthesized using polyimide-coated optical cells. The reactive LC mixture was injected into the polyimide-coated optical cell in the isotropic phase and then slowly cooled down into the nematic phase, followed by UV radiation for 40 minutes. After polymerization, the sample was cooled to room temperature and the optical cell was carefully removed without destroying the formed LCE films. The thermally responsive shape changes of the obtained LCE films were characterized using an Olympus BX53 polarized light microscope equipped with dual polarizers.

The LCE microplates were made following the method reported in previous works.[29,88] Microplate arrays of LCEs were prepared by placing the reactive LC mixture into a PDMS mold covered with a glass substrate to create microplates that are 250 μm long, 50 μm wide, and 200 μm tall. A magnetic field was introduced by placing a magnet (~ 0.4 T) under the PDMS mold. Subsequently, the sample was heated into the isotropic phase, slowly cooled down to the LC phase, and exposed to UV radiation to perform the photopolymerization under a nitrogen atmosphere. After polymerization, the sample was cooled to room temperature and the PDMS mold was carefully removed without destroying the formed LCE microplates. The thermally responsive shape changes of the obtained LCE microplates were imaged by a Zeiss LSM 900 confocal fluorescence microscope. We coated the surface of the LCE microplates with a thin layer of dye, either Rhodamine B or Brilliant Blue, for microscopy imaging.

2.4.8 Molecular Weight Characterization

The molecular weight and distribution of the obtained random LC copolymers were measured by gel permeation chromatography (GPC), using a Viscotek GPC VE2001, equipped with a binary pump, a Viscotek 270 dual detector, and a Viscotek VE 3580 RI detector. The polymers were dissolved in tetrahydrofuran at a concentration of around 1 mg/mL. The molecular weights and polydispersity were derived from a calibration curve based on narrow polystyrene standards. Table 1 in Appendix A summarizes the molecular weight and polydispersity of the synthesized LC (co)polymers in this work.

2.4.9 Nuclear Magnetic Resonance Characterization

The complete consumption of the LC monomers was confirmed through nuclear magnetic resonance (NMR) measurements. The formed LC copolymers were dissolved in deuterated chloroform. A 400 MHz Avance NEO 1H NMR, equipped with an autosampler, was used for the NMR measurements.

2.4.10 X-Ray Characterization

The phase and orientation of the LC functional groups within the LCE were determined by wide-angle x-ray scattering (WAXS). The WAXS system used a Xenocs Inc. Xeuss 2.0 laboratory beamline system with an x-ray wavelength of 1.54 Å. Samples were introduced into a large vacuum chamber to minimize air scattering. Diffraction patterns of LC polymers were recorded using a Pilatus 1M detector (Dectris Inc.) with an exposure time of 1.5 hours and processed using the Nika software package, in combination with WAXSTools wavemetrics Igor. The distance of the emitter was 15 cm from the sample. Furthermore, the scalar order parameter was estimated using the intensity of the π–π stacking of the benzene rings of the LCE (see details in Supporting Information).

2.4.11 Polarized Light Microscopy Imaging and Light Transmission Measurement

The orientation of LC functional groups within the LCE films were recorded using an Olympus BX53 polarized light microscope equipped with dual polarizers. Specifically, we took images of the light transmission of the LCE films while the LC director was at different angles with respect to the dual polarizers and quantified the angle dependent light transmission using ImageJ software to monitor the gray scale (G). 50 μm-thick LCE films with unidirectional planar anchoring were prepared using polyimide-coated optical cells. During the test, the temperature was set to 70 °C and images were taken at 5° intervals under equilibrium conditions. The light transmission of different angles can be calculated as:

$$\text{Transmission (\%)} = \frac{G_{\text{sample}} - G_{\text{sample, min}}}{G_{\text{sample, max}} - G_{\text{sample, min}}} \times \frac{G_{\text{sample, max}} - G_{\text{sample, min}}}{G_{\text{LCM1, max}} - G_{\text{LCM1, min}}} \times \frac{T_{\text{BF, sample}}}{T_{\text{BF, LCM1}}} \times 100 \qquad (1)$$

where G_{sample} is the transmission of polarized light through the LC polymer samples in grayscale, and $G_{\text{sample, max}}$ and $G_{\text{sample, min}}$ are the maximum and minimum transmission of polarized light through the LC polymer samples in grayscale when the LC director is angled 45° relative to both polarizers and parallel to one polarizer, respectively. $G_{\text{LCM1, max}}$ and $G_{\text{LCM1, min}}$ are the maximum and minimum polarized light transmission of the homopolymer of LCM1 in grayscale, respectively. The temperature was set at 70 °C. TBF, sample and TBF, LCM1 are the transmission of unpolarized light (bright field mode) through the LC polymer samples and the homopolymer of LCM1 determined by UV–visible spectrophotometry. Specifically, the light transmission of unpolarized light through the LC polymer samples was measured using a Perkin Elmer Lambda 950 UV–visible spectrophotometer. The light transmission spectra of the LC polymers are shown in Figure 23 in Appendix A. In our calculation, TBF is the average visible light transmission of the LC polymers between 450 nm and 550 nm. The first fraction on the right hand of Equation (1) measures the orientation-dependent light transmission of the LC polymers. The second fraction is used to normalize the light transmission of the LC polymers using a homopolymer of LCM1. The third fraction is used to exclude the interference caused by impurities and the variation in the LC polymer film thickness.

2.5 Results and Discussion

It is known that LCEs made of LC monomers with different configurations can exhibit shape changes in opposite directions with respect to the LC director upon the LC–isotropic phase transition.[27,62,63] The goal of our first set of experiments was to select a pair of prolate and oblate LC monomers for subsequent studies by characterizing thermally triggered shape deformations of their respective LCE homopolymers. Figure 6 shows the molecular structures of the LC monomers that we tested in this work, along with a non-LC crosslinker. Specifically, we used 4-(6-acryloxy-hex-1-yl-oxy) phenyl 4-(hexyloxy) benzoate (LCM1) (Figure 6A), 4-methoxybenzoic acid 4-(6-acryloyloxyhexyloxy) phenyl ester (LCM2) (Figure 6B), 4’’-acryloyloxybutyl 2,5-di(4’-butyloxybenzoyloxy) benzoate (LCM3) (Figure 6C), and non-LC crosslinker 1,6-hexanediol diacrylate (HDDA) (Figure 6D). Arrays of LC homopolymer microplates that were 250 µm long, 50 µm wide, and 200 µm tall were prepared by placing a mixture containing one LC monomer, the photoinitiator, 2-hydroxy-2-methylpropiophenone (DMPAP), and the non-LC crosslinker, 1,6-hexanediol diacrylate (HDDA), into a PDMS mold covered with a glass substrate. A magnet, with a surface magnetic field strength of 0.4 T, was placed under the sample to induce a unidirectional alignment of the LCs along the height of the microplate. Next, the mixture was heated into the isotropic phase and slowly cooled down into the LC phase. Subsequently, the mixture was exposed to UV to initiate photopolymerization. After 40 minutes, the sample was cooled to room temperature and the PDMS mold was carefully removed. We quantified the thermally triggered shape deformations of the obtained LC homopolymer microplates using a confocal fluorescence microscope. It should be noted that in these experiments, the non-LC crosslinker HDDA was added at a concentration of 2.5% by weight relative to the LC monomers to provide a light crosslinking of the linear LC polymer chains, which prevented the melting of the LCE microplates upon the LC–isotropic phase transition. We comment here that such a low concentration of HDDA causes no significant change to the phase diagram, including the phase transition temperatures, of the respective LC polymers, as shown in Figure 24 of Appendix A.

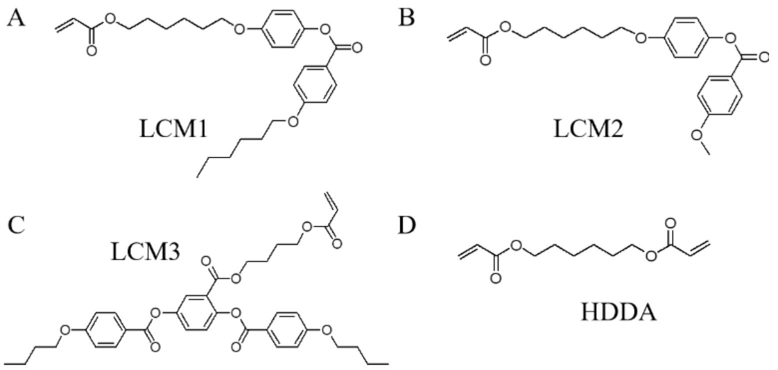

Figure 6. Molecular structure of (A) LCM1, (B) LCM2, (C) LCM3, and (D) non-LC crosslinker used for this research thrust.

Figure 7 summarizes the deformation behavior of microplates of LC homopolymers upon the LC–isotropic phase transition. Microplates of the homopolymer of LCM3 exhibited an ~ 18% uniaxial contraction along the LC director when heated above its LC–isotropic phase transition temperature ($T_{\mathrm{LC-I}}$) (Figure 7B and D), whereas microplates made of LCM1 and LCM2 underwent an ~ 8% (Figure 7A and C) and ~ 4% uniaxial elongation along the LC director, respectively. For the confocal fluorescence images, the surface of the LCE was coated with a thin layer of dye, either Rhodamine B or Brilliant Blue. The colors have been shifted to distinguish the different configurations. L_0 and L_f represent the length of the microplate along the LC director at the initial (90 °C) and final (130 °C) temperatures. No significant hysteresis in the shape deformation of the LCEs as a function of temperature was observed between heating and cooling processes. With wide angle x-ray scattering (WAXS), we confirmed the direction of LC director is always parallel to the magnetic field applied during polymerization for all LC monomers that we used in this study, as illustrated in Figure 25 of Appendix A. According to their characteristic shape changes, we categorized LCM3 as a prolate LC monomer and LCM1 and LCM2 as oblate LC monomers for the other experiments detailed in this chapter.

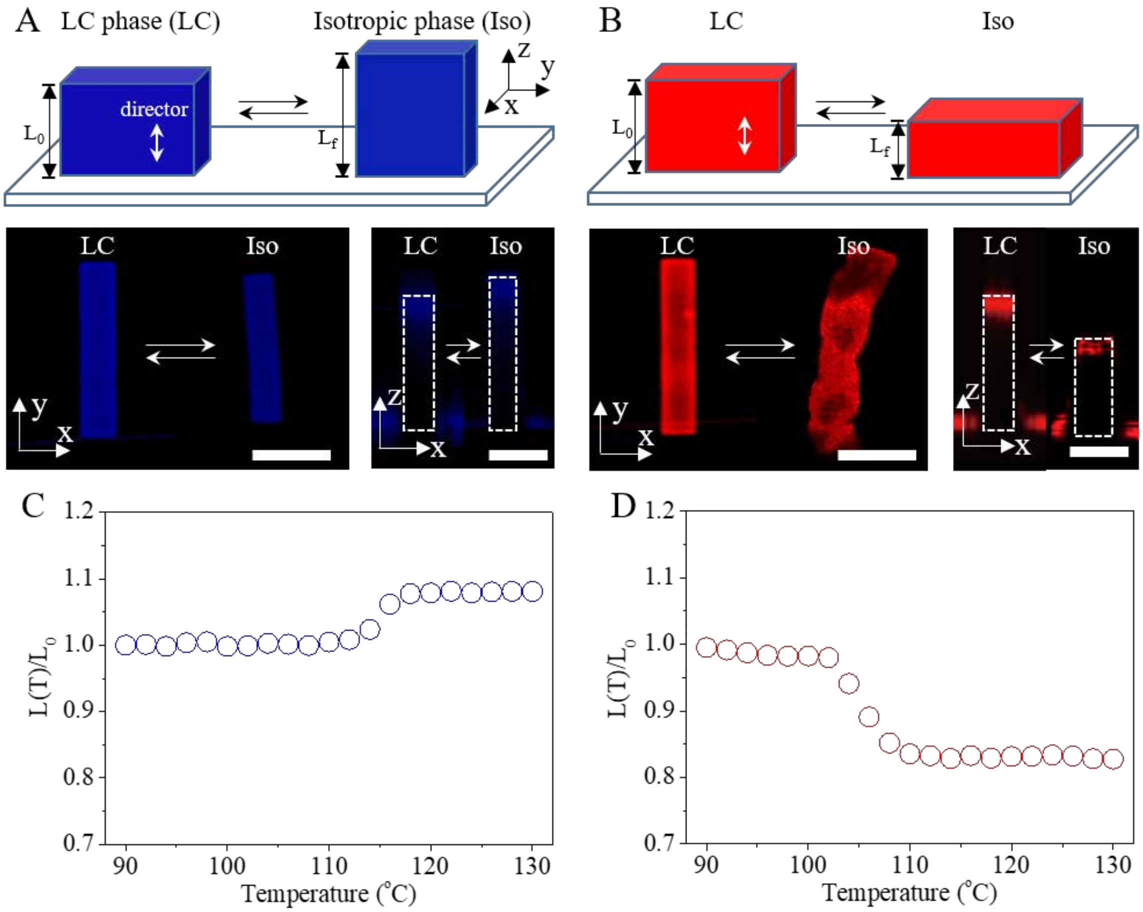

Figure 7. Confocal fluorescence micrographs and accompanying plots of the shape deformation of homopolymer microplate structures of oblate LCM1 (A, C) and prolate LCM3 (B, D) upon phase transition. Scale bars 100 µm.

In the second set of our experiments, we synthesized random copolymers of two LC monomers to investigate the effect of the random sequence, LC monomer configuration, and chemical composition on the phase behaviors of the respective LC copolymers. We synthesized random LC copolymers containing two LC monomers with varying weight percentages. Specifically, the mixture of LC monomers was prepared by dissolving them in dichloromethane at 10% by weight. Photoinitiator DMPAP was added at an amount of

2% by weight based on the total LC monomer mass. Then, photopolymerization was performed for 40 minutes with the use of a UV lamp that delivers 10 mW/cm^2. Next, the solvent was evaporated, and the formed polymer was collected for further characterization. As shown in Figure 26 of Appendix A, the disappearance of the peaks between 5.5–6.5 ppm after the polymerization process in the ^{1}H NMR measurements, corresponding to the non-aromatic C=C double bonds, indicates a full conversion of the reactive LC monomers during photopolymerization. To provide additional evidence to support our assumption of the formation of a random LC copolymer regardless of the reactivity ratios of different LC monomers, we synthesized LC copolymers using RAFT polymerization as control experiments. Past studies have documented that using RAFT polymerization can decrease the chain termination reaction through reversible chain transfer, which enables the synthesis of random copolymers with the same monomer composition as the feed ratios (i.e., truly random).[108-110] As shown in Figure 30 in Appendix A, the phase behavior of the copolymer shows no dependence on the polymerization methods, suggesting the obtained LC copolymer created without using RAFT polymerization has a random chain sequence. In our experiments, the molecular weights of the formed LC (co)polymers ranged from ~17,000 to ~ 27,000 g/mol, as summarized in Table 1 in Appendix A. In future studies, we will use RAFT polymerization to synthesize LC (co)polymers with well-controlled molecular weights and narrow distributions to investigate the effect of molecular weight on the thermomechanical properties of the LC (co)polymers.[108-110]

We then determined the phase diagram of the obtained random LC copolymers by using differential scanning calorimetry (DSC) with a TA DSC Q100 instrument. The first set of copolymers was the combination of the same configuration of LC monomers – oblate LC monomers LCM1 and LCM2. Figure 8A and Figure 27A of Appendix A show the $T_{\mathrm{LC–I}}$s of the random LCM1–LCM2 copolymers as a function of chemical composition. We found that each random LCM1–LCM2 copolymer possesses a single $T_{\mathrm{LC–I}}$, and over the whole chemical composition range, the $T_{\mathrm{LC–I}}$s of the LCM1–LCM2 random copolymers lie between the $T_{\mathrm{LC–I}}$s of the respective homopolymers, those being 115 °C and 90 °C for LCM1 and LCM2 homopolymers, respectively. For example, the transition temperature of the 20/80 mixture of the two oblate monomers LCM1 and LCM2 was found to be around 100 °C. This observed trend is similar to numerous non-LC random copolymers such as poly(ethyl-hexyl-acrylate-*r*-n-butyl acrylate) (EHA–nBA) and poly(ethyl acrylate-*r*-methyl acrylate) (EA–MA), the glass transition temperatures (T_gs) of which lie between those of the respective non-LC homopolymers. To provide an additional insight, we measured the phase behaviors of unpolymerized mixtures of LCM1 and LCM2. Figure 8B shows that the $T_{\mathrm{LC–I}}$s of the unpolymerized mixtures lie between the $T_{\mathrm{LC–I}}$s of the respective monomers, similar to what was observed with the random LCM1–LCM2 copolymer. The fact that only one transition temperature was observed for the LC monomer mixtures suggests that there was no phase separation between the different LC monomers. This finding, in combination with the DSC results from the copolymers, indicates that the effects of the random chain sequence on the thermal properties of the LC copolymers consisting of the same configuration of LC monomers are similar to most of the conventional non-LC random copolymers. We note here that in contrast to the random LCM1–LCM2 copolymers with only one $T_{\mathrm{LC–I}}$, the homopolymer mixtures of LCM1 and LCM2 show two individual $T_{LC–I}$s corresponding to those of each homopolymer, suggesting a phase separation in the homopolymer blend (see Figure 28A of Appendix A).

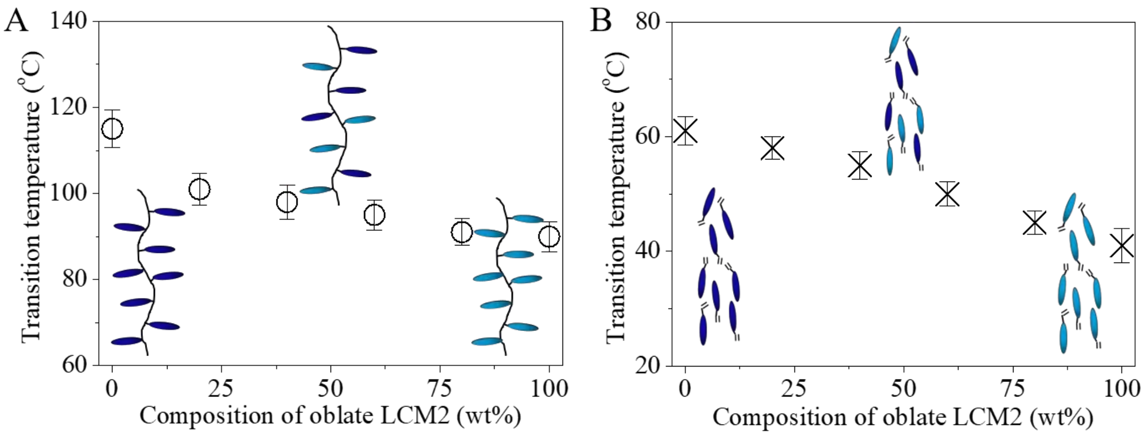

Figure 8. Liquid crystal to isotropic phase transition temperatures of a random copolymer and unpolymerized monomer mixtures consisting of two oblate monomers. Darker blue corresponds to LCM1 and lighter blue corresponds to LCM2.

Next, we characterized the thermal properties of random copolymers consisting of different configurations of LC monomers, specifically between the oblate LCM1 and the prolate LCM3. A single $T_{LC–I}$ exists in every random LCM1–LCM3 copolymer, as shown in Figure 8A and in Figure 27B of Appendix A. Surprisingly, in contrast to the random copolymer of LCM1–LCM2, the $T_{LC–I}$s of LCM1–LCM3 random copolymers lie below the $T_{LC–I}$s of the respective homopolymers, 115 °C and 107 °C for LCM1 and LCM3 homopolymers, respectively. For example, a transition temperature around 80 °C was found for the 20/80 mixture of oblate monomer LCM1 and prolate monomer LCM3. This decrease in the $T_{LC–I}$s of the random LCM1–LCM3 copolymers may hint that the interaction and orientational order of the LC functional groups may have been diminished.

In addition, a mixture of homopolymers of LCM1 and LCM3 exhibited two T_{LC-I}s, suggesting phase separation of two different LC homopolymers in the mixture, as can be seen in Figure 28B of Appendix A. This observation, combined with the single T_{LC-I} in the copolymer, rules out the possibility of phase separation within the random LCM1–LCM3 copolymers.

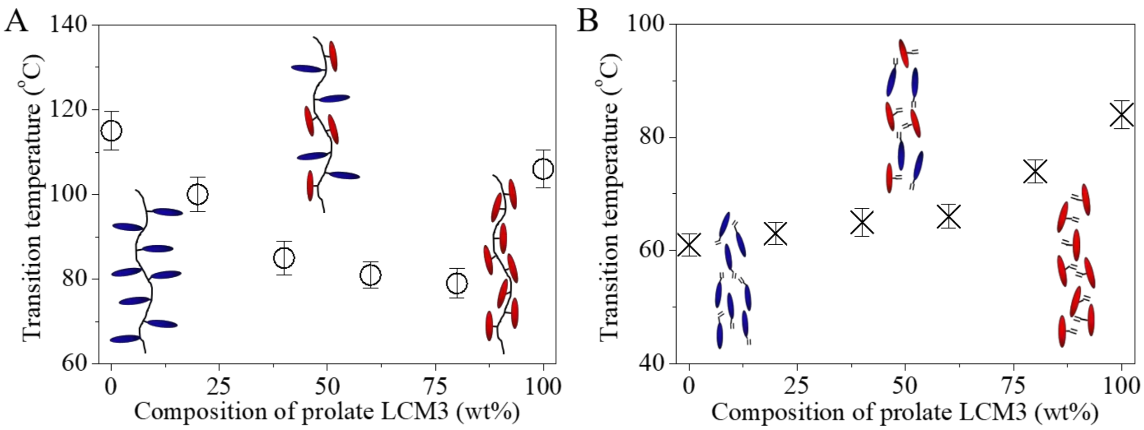

Figure 9. Liquid crystal to isotropic phase transition temperatures of a random copolymer and unpolymerized monomer mixtures consisting of an oblate and prolate monomer pair. Darker blue corresponds to LCM1 and red corresponds to LCM3.

To better illustrate the diminished orientational order between the pendant LC groups in random copolymers made of different LC monomers, we measured the light transmission of the surface-aligned, uniaxially oriented LC (co)polymeric films. 50 µm thick LC (co)polymeric films were synthesized using polyimide-coated optical cells. The light transmission through the LC (co)polymeric films when the LC director is at different angles with respect to the direction of the crossed polarizers was taken at 70 °C and was quantified using ImageJ software. As can be seen in Figure 10, LCE films made of LCM1 and LCM3 homopolymers and LCM1–LCM2 random copolymer exhibit similar light transmissions. However, the magnitude of the light transmission of the random LCM1–LCM3 copolymer is greatly reduced at all angles with respect to the crossed polarizers. In addition, we used WAXS to estimate the scalar order parameter of the above polymers to be ~ 0.250 (homopolymer of LCM1), ~ 0.275 (homopolymer of LCM3), ~ 0.278 (random copolymer of LCM1–LCM2) and ~ 0.102 (random copolymer of LCM1–LCM3). We note here that the scalar order parameter of the homopolymers is consistent with previous studies.[85] The composition of LCM1 in the copolymers was 40% by weight. The x-ray analysis, combined with the light transmission results, confirmed that the orientational order of the random LCM1–LCM3 copolymers was greatly diminished compared with the respective LC homopolymers and random copolymers of the same configuration of LC monomers (i.e., LCM1–LCM2). For more information on the calculation of the scalar order parameter, please see Appendix A around Figure 25.

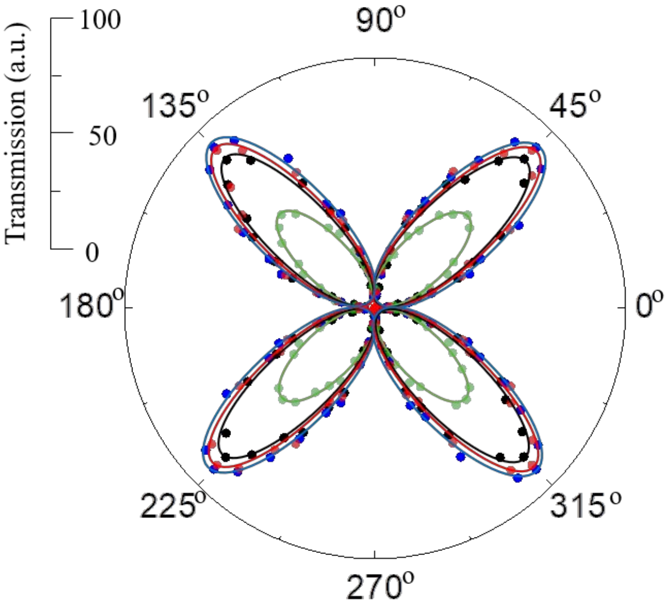

Figure 10. Light transmission through the homopolymers of LCM1 (blue) and LCM3 (red) and the random copolymers of LCM1–LCM2 (black) and LCM1–LCM3 (green) in the LC state at 70 °C between crossed polarizers set at 0° and 90°, respectively.

A previous study on non-LC random copolymers, specifically poly(methyl methacrylate-*r*-vinyl chloride) (MMA–VC) and poly(methyl methacrylate-*r*-acrylonitrile) (MMA–AN), reported that weakened interactions between different monomers can lower phase transition temperatures of the copolymers below those of the respective homopolymers.[111] Building on these previous findings, we hypothesized that the interactions between different configurations of LC monomers (LCM1–LCM3) are diminished, resulting in a disruption of the orientational order of the LC functional groups. However, this does not appear to be the case in random LCM1–LCM3 copolymers as no phase separation was seen in the mixtures of the LC monomers, suggesting no measurable reduction in the interaction between LCM1 and LCM3. Moreover, as shown in Figure 9B, the $T_{\text{LC–I}}$s of the unpolymerized mixtures lie between the $T_{\text{LC–I}}$s of the pure monomers

LCM1 and LCM3, unlike what was observed with the random copolymers of the two monomers. These results allude to some other interactions causing the decrease in the T_{LC-I}s of copolymers of different LC monomers.

The previous study also showed that the contributions of diad- and triad-sequences to the T_g can be used to extend the Gordon–Taylor equation based on volume additivity to explain the asymmetric T_gs as a function of composition of binary random copolymers.[112] We used this extended Gordon–Taylor equation to quantify the deviation of the T_{LC-I}s of the unpolymerized LC mixtures and the LC random copolymers from additivity because of specific interactions between the LC repeating units (Equation 2):

$$(T_{LC-I} - T_{LC-I,1}) / (T_{LC-I,2} - T_{LC-I,1}) = (1 + K_1)\, x_2 - (K_1 + K_2)\, x_2^2 + K_2\, x_2^3 \qquad (2)$$

in which x_2 is the weight fraction of the second component of the random LC copolymers, K_1 and K_2 are the fitting parameters of the composition power, and $T_{LC-I,1}$ and $T_{LC-I,2}$ are the T_{LC-I}s of the respective LC homopolymers. K_1 has been shown to depend on the contributions of the hetero-diads to the T_g of the random non-LC copolymers. When the interactions and contributions of the repeating units in a random copolymer are equal to those found in a homopolymer, K_1 is found to be close to 0. $K_1 > 0$ indicates positive deviations of the random copolymer T_g from additivity, suggesting strengthened interactions between the repeating units of the hetero-diads. In contrast, $K_1 < 0$ suggests correspondingly negative deviations from the additivity of the random copolymer due to weakened interactions within the hetero-diads. In our experiments, we used Equation (2) to obtain the K_1 for the random LC copolymers. As shown in Figure 11, for the same configuration of LC monomers (i.e., LCM1–LCM2), the K_1 values of both unpolymerized

LC monomer mixture and the respective random LC copolymers are ~ 0, which suggests that the $T_{LC–I}$s of the LCM1–LCM2 random copolymers lying between those of the respective homopolymers can be explained by the interactions between the LC pendant groups in the copolymer being nearly equivalent to the interactions between those in the homopolymers.

For different configurations of LC monomers, specifically the LCM1–LCM3 pair, the K_1 value of the unpolymerized monomer mixtures of the different configurations of LC monomers are approximately 0, suggesting that the interactions between LCM1 and LCM3 pendant groups in the random copolymer are equal to those found in the respective homopolymers. After polymerization, however, the negative K_1 value suggests a negative deviation from the simple additivity of the random LCM1–LCM3 copolymer, which is similar to MMA–VC and MMA–AN. These results lead us to hypothesize that attractive dipole–dipole interactions and the π–π stacking of the benzene rings exist in both oblate and prolate LC monomers and is dominant in the mixtures of LC monomers, while after polymerization, the steric hindrance of different configurations of LC mesogens and the limited flexibility of the polymer backbones prevents the pendant LC moieties to closely pack and form well-ordered materials, resulting in a weakened interaction between the oblate and prolate LC moieties and a consequent decrease in the $T_{LC–I}$ of the respective copolymers. To verify our hypothesis, we synthesized and characterized random copolymers of another pair of prolate and oblate LC monomers – LCM2 and LCM3. As shown in Figure 29 Appendix A, the $T_{LC–I}$s of the LCM2–LCM3 random copolymers lie below that of both respective homopolymers, while the $T_{LC–I}$s of the LCM2–LCM3 monomer mixtures lie between those of the respective monomers. These features are similar to the random copolymers of LCM1 and LCM3. Overall, these results lead us to conclude that a statistically random distribution of prolate and oblate LC monomers along a polymer backbone disrupts the orientational order of the pendant mesogenic groups of the formed LC copolymers, whereas random copolymers of the same configuration of LC monomers preserves the orientational order of the constituent mesogenic functional groups.

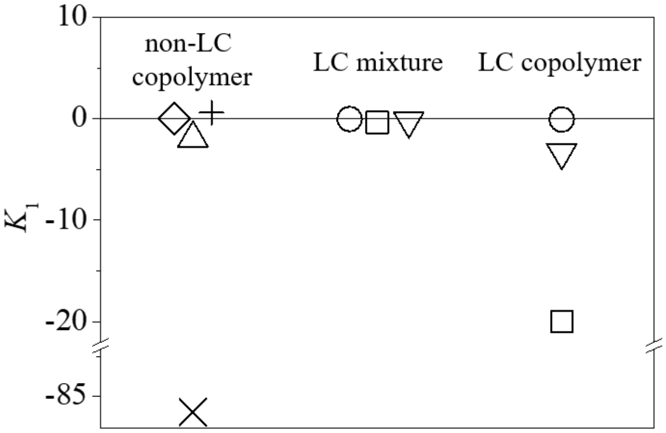

Figure 11. Fitting parameter K1 of Equation (2) for non-LC random copolymers, LC monomer mixtures and random LC copolymers: LCM1–LCM2 (circles), LCM1–LCM3 (squares), LCM2–LCM3 (down triangles), MMA–AN (crosses), MMA–VC (up triangles), EA–MA (plusses) and EHA–nBA (diamonds).

In our final set of experiments, we sought to determine the effect of a random chain sequence on the deformation behavior of the LC copolymers. A microplate array of random LC copolymers was prepared by placing mixtures of LC monomers, photoinitiator DMPAP, and non-LC crosslinker HDDA into a PDMS mold covered with a glass substrate.

The samples were heated to the isotropic phase and slowly cooled down to the LC phase, followed by UV-induced photopolymerization in the presence of a vertically aligned magnetic field. After 40 minutes, the samples were cooled to room temperature and the PDMS molds were carefully removed. The thermally triggered shape deformation of the obtained random LC copolymer microplates was measured using confocal fluorescence microscopy.

Figures 12 and 13 illustrate the shape deformation of random copolymer microplates, consisting of different configurations of LC monomers. Interestingly, the thermally triggered shape changes of the LCM1–LCM3 microplates can be continuously tuned from ~ 8% elongation to ~ 18% contraction along the mesogenic director (z-axis) by increasing the composition of prolate LCM3 from 0% to 100% in the heating process. Figure 12 shows confocal fluorescence micrographs showing the shape deformation of microplate structure of LCM1-LCM3 random copolymers upon a LC-isotropic phase transition as a function of monomer composition. Figure 12A shows a microplate at 70 °C and Figure 12B-D show the material in the isotropic phase (110 °C). The LCM1 compositions are (B) 75%, (A,C) 50%, and (D) 25% by weight for Figure 12. Figure 12E shows a plot of the representative dimensional changes of the LCE microplates along the director (z direction) as a function of temperature. LCM1 compositions are 75% (cross), 50% (circle), and 25% (triangle) by weight. Moreover, the extent of the uniaxial deformation as a function of copolymer chemical composition yielded a nearly linear relationship, as shown in Figure 13. We hypothesize that the tunable deformation behavior is caused by the different coupling interactions between pendant LC functional groups and the polymer backbones for prolate and oblate LC monomers, which results in the monomer configuration- and composition-dependent shape deformation of the respective random LC copolymers. To verify our hypothesis, we synthesized and characterized microplate structures consisting of the same configuration of LC monomers. In contrast to the transition of deformation from elongation to contraction for LCM1–LCM3 copolymeric structures, LCM1–LCM2 microplates always exhibited thermally induced uniaxial elongation with respect to the LC director (z-axis) over the whole composition range, as summarized in Figure 13. These observations not only support our hypothesis that the LC monomer configurations and the composition of the copolymer affect the magnitude and direction of the deformation of a formed LCE, but more importantly, hint at a novel route to program the shape deformation of the LCE.

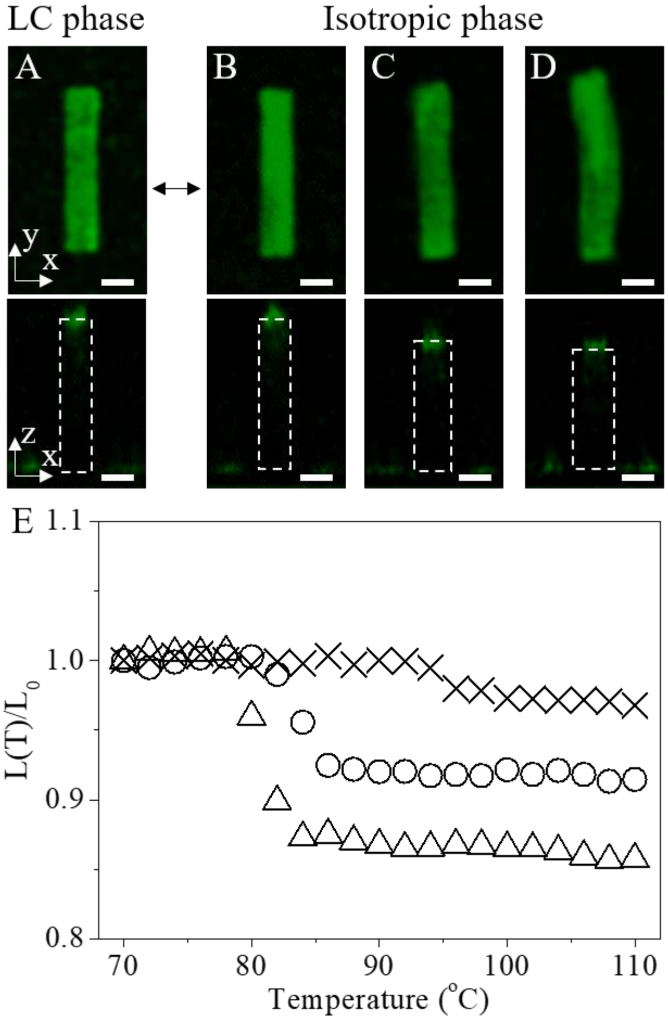

Figure 12. Confocal fluorescence micrographs and accompanying plot showing the shape deformations of LCM1-LCM3 random copolymers. Scale bars, 50 µm.

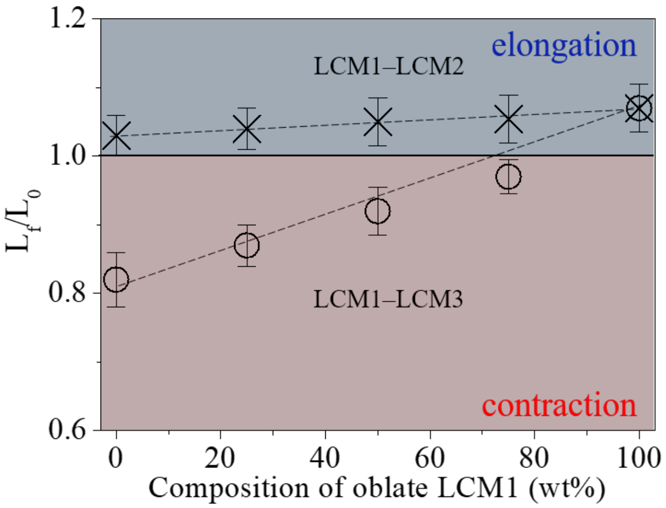

Figure 13. Uniaxial deformation of LC copolymeric microplates with respect to LC director as a function of chemical composition and monomer configuration (cross: LCM1–LCM2; circle: LCM1–LCM3).

I end this chapter by commenting on the potential application that might be enabled by our findings from this work. Past studies have demonstrated that the precise control over the internal LC orientation serves as one of the key methods to manipulate the deformation behaviors of LCEs made from a single configuration of LC monomer.[28,103,113-117] This understanding has led to the use of a variety of patterned surfaces to manipulate the bulk equilibrium alignment of the LC functional groups to achieve complex patterned shape deformations of the LCE.[26] Current techniques that have been reported for the preparation of a patterned substrate for LC alignment include patterned rubbing and photoalignment.[93] While promising, these methods typically require complex procedures or expensive equipment. Additionally, these methods are challenging to perform on large scales and in three dimensions.

We believe that the results reported in this chapter substantially advance our understanding of how the LC monomer configurations and chemical compositions influence the deformation behaviors of random LC copolymers. Based on these findings, we propose a novel method to achieve patterned complex deformations of LCEs without requiring either complex procedures or expensive equipment. Specifically, by simply applying a uniform external field to set a constant LC director over the whole LCE structure, we can program local deformation behaviors by patterning the chemical composition of the reactive mixture of prolate and oblate LC monomers, as illustrated in Figure 14. We predict that the regions with a high ratio of oblate or prolate LC monomers would lead to elongation or contraction along the LC director, respectively.

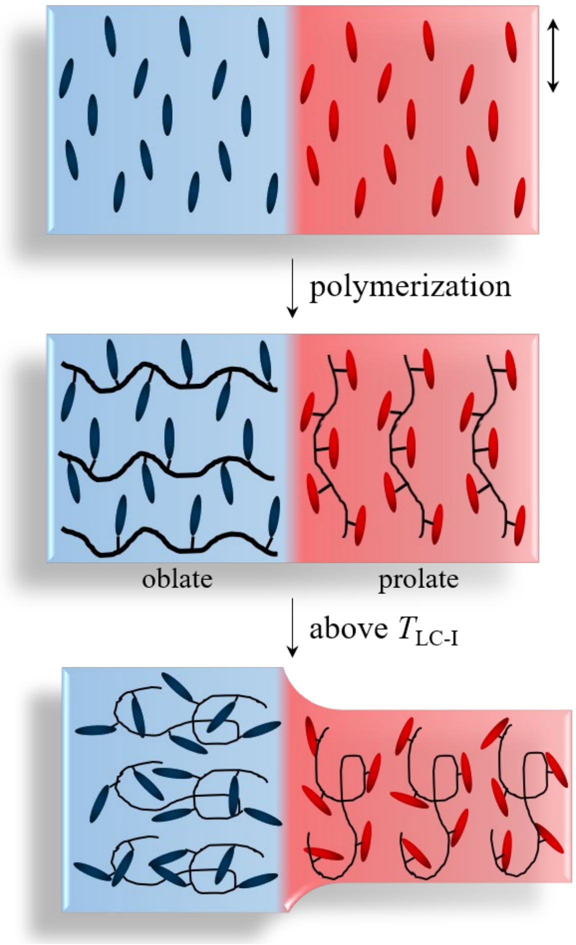

Figure 14. Control over the deformation behavior of LCEs through patterning LC monomers with different configurations. The double-headed arrow indicates the LC director.

To verify our hypothesis, we used a stepwise polymerization process to produce LCE structures possessing non-uniform, area-specific deformations defined by their spatial LC monomer configuration. Each step followed a similar method to what was used to create the other LCE structures, with the first mixture being composed of oblate LCM1, HDDA at 2.5% by weight based on LCM1, and DMPAP at 2% by weight based on LCM1 and the second mixture being composed of prolate LCM3, HDDA at 2.5% by weight based on

LCM3 and DMPAP at 2% by weight based on LCM3. The block of LCM1 was created first in the nematic phase with a subsequent step to create the block of LCM3 in the nematic phase. For this polymerization, an optical cell composed of polyimide-coated glass slides was used to provide the uniform LC alignment. This is expected to create a parallel alignment of the different LC monomers.

The mesogenic orientation within the formed LCM1–LCM3 polymeric structure was characterized using an Olympus polarized light microscope. A uniform dark appearance was observed in the whole polymeric structure when the long axis of the polymeric structure was parallel to one of the polarizers, whereas a bright optical appearance was visible in both of the LCM1 and LCM3 domains when the polymeric structure was aligned at 45° with respect to the crossed polarizers, as seen in the micrographs in Figure 15A and 11B. Upon heating into the isotropic phase, the LCM1 and LCM3 domains deformed in the opposite direction with respect to the LC director, as demonstrated in Figure 15C and 11D. This observation further cements our hypothesis that the LCs are aligned parallel to each other as we would expect to see the same direction of deformation from perpendicularly aligned prolate and oblate LCEs. Overall, the results from our research provide the basis for a novel and facile technique that can be used to program the spatial deformation behavior of LCEs, which can be complemented by 3D printers equipped with multiple printing nozzles to precisely control the spatial chemical composition of the LC monomers. We expect these materials to find use in soft robotics as artificial muscles or soft actuators where opposite deformation directions are needed. For example, this type of material could be used to alternate the contraction of two separate actuators with only one signal as the two parts of the material deform in opposite directions in response to a single stimulus.

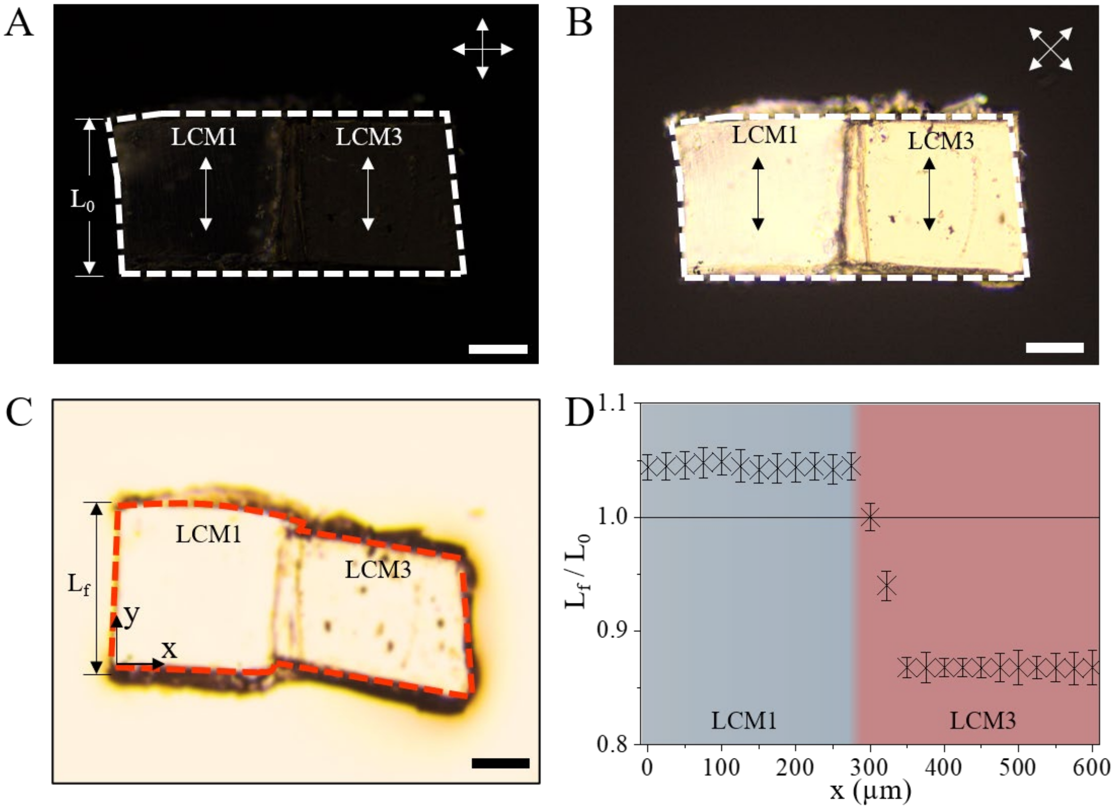

Figure 15. (A-C) Polarized optical micrographs of patterned copolymer structure and (D) plot of the deformation of the material as a function of position along the material. Scale bars 100 µm.

2.6 Conclusion

The results reported in this chapter provide fundamental insight into the effects of the coupling between the pendant LC moieties with different configurations (oblate and prolate), which guides the design of a novel class of shape changing polymers based on liquid crystalline random copolymers. In particular, within LC copolymers, a statistically random distribution of prolate and oblate LC monomers disrupts the orientational order of the pendant mesogenic groups, whereas random copolymers of the same configuration of LC monomers preserves the orientational order of the constituent mesogenic functional groups. More importantly, we find that the shape changing behavior of the formed LC random copolymers can be manipulated by pattering the local chemical composition of prolate and oblate LC monomers, which hints at a novel and facile way for the synthesis of LCEs with complex shape deformations. We comment here that our prolate LC monomer, also known as a side-on side-chain LC monomer, has limited selection, and synthesis of side-on LC monomers with different molecular structures is being investigated. In future studies, we will synthesize side-on LC monomers with different aliphatic chain lengths between the acrylate functional group and the LC moiety and will investigate their effect on the thermomechanical properties of LC copolymers. Overall, the results reported in this chapter demonstrate that the monomer configuration and polymer composition indeed affect the mechanical and thermal properties of LCEs, thus expanding the phase diagram and deformation behavior of the LCEs that can be synthesized. Future efforts will be extended to more complicated chain architectures, including block and gradient structures, that may find use as the basis of novel responsive soft materials. Particularly, when combined with the recent advances in the synthesis of LCEs with reversible crosslinking covalent bonding that have emerged over the past decade, our method may present many opportunities for the design of responsive polymeric materials and structures with complex shape deformation behaviors in three dimensions.

Chapter 3 Stimuli responsive liquid crystal elastomers with densely packed, friction amplifying nanowire structures for soft robotics

3.1 Preface

This chapter comes from a manuscript being prepared for submission to *Advanced Materials* in 2024. It is focused on the creation of nanoscopic surface structures to enhance the properties, specifically the adhesion, of liquid crystal elastomer films. This would help them find extra use in soft robotics as it still maintains their reversible stimuli-responsive deformations.

3.2 Abstract

Nature provides many examples of the benefits of nanoscopic surface structures in areas of adhesion and antifouling. For instance, the surface structures on the footpads of geckos have been shown to increase their adhesion to surfaces. We utilized anodized aluminum oxide templates during polymerization to create nanoscopic surface structures, namely nanowires, on liquid crystal elastomer films. The nanowires increased the adhesion of the films to a variety of surfaces, including glass and plastics, allowing the films to hold an increased amount of weight. In addition, by controlling the orientation of the liquid crystal monomers during polymerization, we created films that curl towards the nanowires increasing the surface contact of the films to curved surfaces. Finally, by patterning the location of the nanowires on the surface, we can create materials that locomote in response to stimuli.

3.3 Introduction

Researchers have looked to nature for inspiration to design advanced materials for more complex applications. Some of these inspirations include the antifouling surface structures of lotus leaves,[118-120] the surface actuation found on Mako shark fins,[121,122] and the adhesive capabilities of geckos.[35,36,123] With respect to gecko's feet, many researchers have focused on replicating the unique, hierarchical structure of the hairs on their footpads. Specifically, hundreds of thousands of microscopic pillars, called setae (approximately 90 μm long and 10 μm in diameter), on the gecko's feet, each ending with hundreds of even smaller spatula shaped structures (approximately 20 μm long and 0.2 μm in diameter), seen in Figure 16A, drastically increase the contact surface area of the gecko's feet.[123] This large surface area leads to an increase in the van der Waals forces between the gecko and the surface which provides for the enhanced adhesion.[35,36] Many of these structures use flexible films with polymeric micropillars on one side, relying on a more simplistic model of the gecko's foot,[82,124-127] whereas a few other structures use nanoscale materials, like carbon nanotubes,[128] to better mimic the structure of the gecko's foot. However, many of these materials are unresponsive to external stimuli which limits their application in soft robotics.

Soft robotics utilizing shape-memory polymers (SMPs) have drawn a great deal of attention owing to their unique properties including controlled deformability, high durability, and unparalleled adaptability.[17,58,129,130] An extraordinary amount of progress in soft robotics has been seen in recent years, from the synthesis methods[131,132] and material selection[18,133] to the design of complex architectures[134,135] and 4D printing.[53,136] More recently, researchers have begun to use stimuli-responsive liquid crystal elastomers

(LCEs).[27,62] LCEs take advantage of the self-assembly of liquid crystal (LC) moieties to create stimuli responsive materials. By polymerizing and crosslinking together LC monomers, researchers can create polymer chains that are trapped in a thermodynamically unfavorable stretched conformation, with the favorable random coil conformation attainable upon a LC to isotropic transition of the LC moieties. This causes a macroscopic deformation in the material that is responsive to external stimuli. This deformation can be reversed back to the stretched conformation by cooling the material back down beyond the LC to isotropic transition. The incorporation of these LC materials and their reversible, stimuli-responsive deformations has widened the applications of SMPs into areas of sensing,[63,137,138] actuating,[29,63,83] and drug delivery.[139-141]

In this chapter, I present a one-pot synthesis method to create LCEs with densely packed, friction amplifying nanowire structures on the surface that are on the order of the spatula shaped structures on the gecko's foot. Specifically, we utilize an anodized aluminum oxide (AAO) template and a mixture of a reactive LC and LC crosslinker to create LCE films with densely packed nanowires on the surface that are 10 μm long and 400 nm in diameter. To the best of our knowledge, this is the first time that LCEs have been made directly with nanowire structures on the order of gecko feet setae. Our materials are shown to be responsive to both heat and solvent stimuli while also showing an increase in the frictional adhesion caused by the nanowire structures. More importantly, we demonstrate the synergistic effect of the two material properties by combining the curling motion that is easily attained with LCEs with the increased adhesion from the nanowires to grab curved surfaces.

3.4 Experimental Section

3.4.1 Materials

The following LC monomers were purchased from Synthon Chemicals Ltd.: 4-(6-Acryloxy-hex-1-yl-oxy)phenyl 4-(hexyloxy)benzoate (end-on) and 1,4-bis-[4-(3-acryloyloxypropyloxy)benzoyloxy]-2-methylbenzene (RM257). The following chemicals were purchased from Sigma-Aldrich: 100 cSt silicone oil, 2,2-dimethoxy-2-phenylacetophenone (DMPAP), dimethyloctadecyl [3-(trimethoxysilyl)propyl] ammonium chloride (DMOAP), poly(pyromellitic dianhydride-co-4,4'-oxydianiline) amic acid, 1-methyl-2-pyrrolidinone, and toluene. Plain microscope slides (25 mm × 75 mm × 1 mm) were purchased from Fisher Scientific. Unless stated otherwise, purchased chemicals and materials were used as received without further modification or purification.

3.4.2 Nanowire Augmented Liquid Crystal Elastomer Film Creation

First, we prepared a polyimide (PI) coated glass slide by spin coating a PI solution on a glass slide at 2000 rpm. This glass slide was then heated at 350 C for 2 hours before rubbing the coated side with velvet to create the planarly aligning PI coated glass slide. We then placed an AAO template on a separate, uncoated glass slide along with two spacers. This was preheated at 65 C while the following steps were performed. A mixture of 90 wt% end-on and 10 wt% RM257 was mixed together and heated at 80 C to melt. Mixing was done through vortex. Then, an addition 1 wt% of the photoinitiator, DMPAP, was added to the mixture before mixing briefly with vortex. This mixture was then pipetted onto the AAO template and was allowed to sit for 10 minutes so that the mixture could fill the nanovoids in the template. The PI coated glass slide was placed on top and the optical cell was clipped together where the spacers were. This was then polymerized with 365 nm UV at 10 mW/cm^2 for 15 minutes. Once done, the glass slides were separated and the back of the AAO template was scratched with a pair of tweezers. The AAO template, LCE film, and attached glass slide were then placed in 12 M HCl until the AAO template was fully etched away, usually around 4 days. Finally, the film was taken from the HCl, washed with water, and dried for further testing.

3.4.3 Temperature Activated Deformation Testing

A strip of film approximately 10 mm long and 2 mm wide was cut with a scalpel from the larger film. This strip was then put into a beaker of silicon oil on a hotplate. A thermometer was placed into the silicon oil to accurately measure the temperature. The temperature of the hotplate was then changed and allowed to stabilize before a picture of the film was taken. The mean curvature of the curling film was then measured using a homemade MATLAB program. The program was designed to capture the pixel information of the surface of the film to calculate the curvature.

3.4.4 Solvent Activated Deformation Testing

A strip was cut from the full film as before. For the solvent vapor deformation testing, the film was gently grasped by the arms of a binder clip which was then placed on its side. This was done to hold the film strip above the surface of the table. A pool of solvent was placed below the film making sure that the film did not touch the solvent. A crystallizing dish was then placed over top of the film and pool of solvent to trap the solvent vapor. A video of the film was taken and was fed into the same MATLAB program to be analyzed.

The program was designed to take frames from the video every 10 seconds to speed up processing and analysis.

For the solvent droplet deformation testing, the film was again gently grasped by the arms of a binder clip which was then placed on its side to hold the film off the table. Then, a droplet of solvent was carefully placed on the edge of the film. A video of the film was taken like before and the curvature of the films were analyzed in MATLAB.

3.4.5 Adhesion Testing

A strip of nanowire film was cut from a larger sample. The film was then pressed onto a surface using a known weight. To apply an even and controlled force over the entire sample, a small baggie was placed over the sample and filled with water. This worked for both flat and curved surfaces. Next, tape was used to attach a string to the film and a known weight was attached to the string. The surface was then lifted until the weight was hanging freely from the film. The force used to adhere the film and the force the film could hold up were then compared. To adhere to curved surfaces, the temperature of the film was raised in an oven. The same procedure above was followed but setup took place in an oven. For the solvent-based adhesion testing, small amounts of solvent were applied to the films to curl them away from the nanowire side to help the films adhere to oppositely curved surfaces. Otherwise, the procedure was the same.

3.5 Results and Discussion

To create our bioinspired nanoscopic surface structures, inspired by those seen in Figure 16A, we first prepared an anodized aluminum oxide (AAO) template inside of an optical cell. We did this by placing the template on a glass slide with a spacer on either side. The spacers were thicker than the template and were used to control the thickness of the resulting film. The nanowire dimensions were controlled by the size of the pores in the template. Figure 16B shows a representative SEM image of the top and side of the templates. Most of the results in this work have nanowires that are 10 µm long and 400 nm in diameter. This construction was placed on a hotplate at 60 C to warm up while the mixture was prepared. Once warm, the reactive LC mixture was placed on the surface of the template and allowed to soak into the pores for 10 minutes. Then, the optical cell was closed with a PI coated glass slide and a pair of binder clips were positioned over where the spacers were. The reactive mixture in the cell was exposed to UV to induce photopolymerization. The cell was then carefully broken apart and the film was left adhered to the PI coated glass slide. The backside of the template was heavily scratched with laboratory tweezers to remove some excess mass and to increase the surface area before being place in hydrochloric acid for five days to etch away the remaining AAO. Once fully etched, the film was removed from the acid and was washed with MilliQ water to remove any excess acid. The resulting film was then used for all analysis. A schematic of this process and the LC monomers used in this study can be seen in Figure 16C. The nanowires on the surface of the film create a dull texture, whereas the base film is otherwise shiny. A representative image of the created films can be seen in Figure 16D, and SEM images of the nanowires on the surface of the film can be found in Figure 16E.

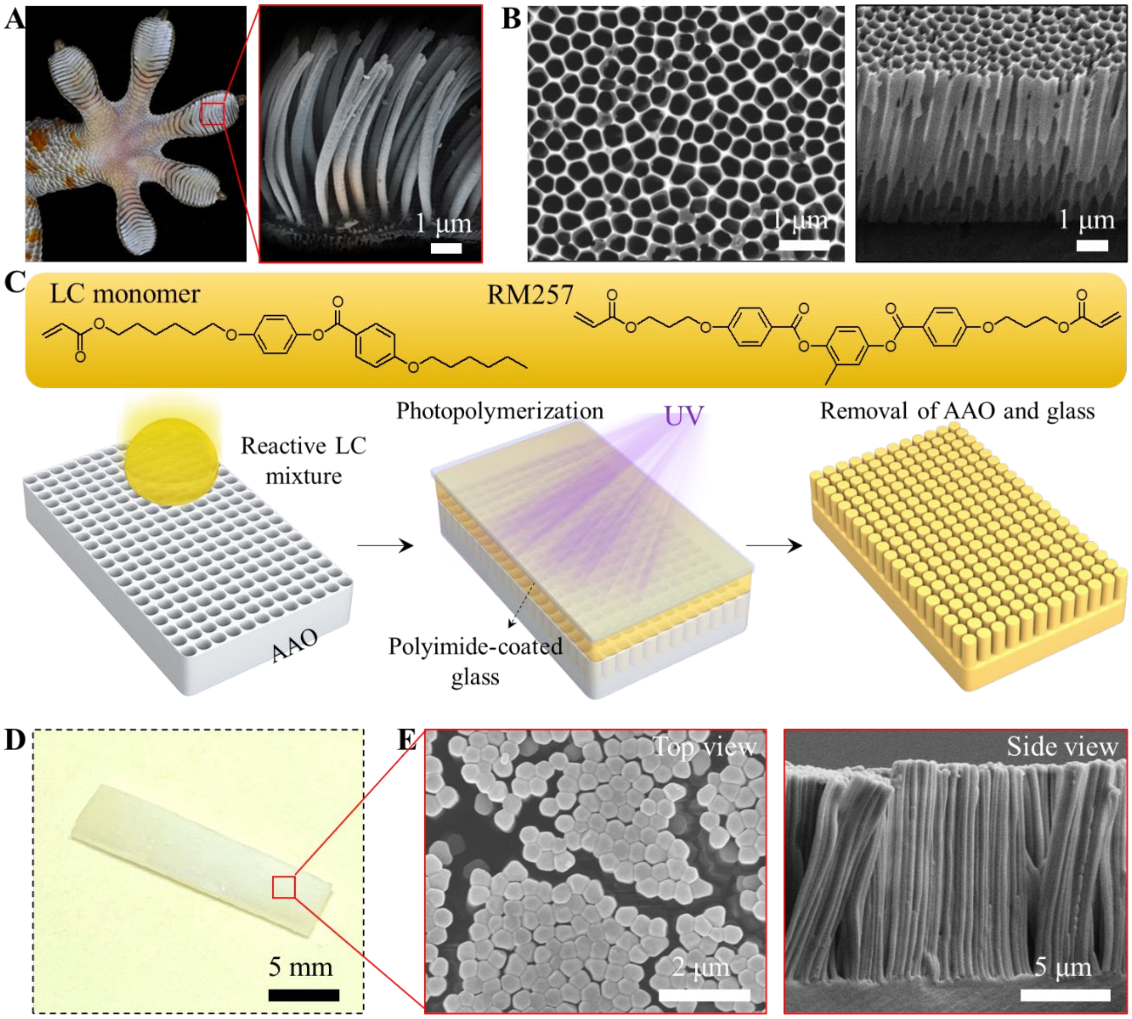

Figure 16. Nanowire augmented liquid crystal elastomer film motivation, creation, and characterization including SEM and regular images of the nanowire films.

After polymerization, we investigated the alignment of the liquid crystal moieties in the nanowires and the film. This also included investigating the stimuli-responsive deformation of the materials. Individual nanowires show the tell-tale bright-dark transition upon rotation between crossed polarizers pointing towards a unidirectional alignment (Figure 17A). Brightfield images are provided for additional clarity regarding the direction of the nanowire between the polarizers. Clusters of nanowires also exhibit the bright-dark transition upon rotation. Figure 17B shows the deformation of an individual nanowire upon heating above the nematic to isotropic phase transition temperature ($T_{N\text{-}I}$ ~ 55 °C). As can be seen, the nanowires appear to elongate by about 5% when heated. This slight deformation is common for end-on type LCEs, and the aspect ratio of the nanowires paired with the direction of the polymer chain hamper large deformations in the nanowires. Combining the deformation direction and the POM images, we believe the LCs are aligned along the length of the nanowires, as visible in the associated schematic. This aligns with other work that created standalone LCE nanowires with side-on type LC monomers.[142]

Looking at the whole film, when heated above the $T_{N\text{-}I}$ of the LCE, the film curls in the direction of the nanowire, shown in the images, plot, and scheme in Figure 17C. Because of the alignment provided by the AAO template nanopores, the surface of the film on the nanowire side also aligns perpendicularly to that side of the film, whereas the PI coating on the opposite glass slide provides a parallel alignment, as seen in Figure 17D. This causes the polymer chains to align in opposite directions on the two sides of the film which in turn causes the curling deformation seen. This curling deformation begins at the $T_{N\text{-}I}$ and continues until around 150 °C where it hits a high temperature plateau. The maximum mean curvature of the film depends on the thickness of the film, with thicker films curling less than thinner films, as seen Figure 31 of Appendix B. The curling is also totally dependent on the alignment of the polymer chains in the film and is not significantly impacted by the nanowires, as seen in Figure 32 of Appendix B, where the same film curls approximately the same amount before and after the nanowires were removed from the surface. The nanowires were carefully removed so that there was a negligible impact on the thickness of the film.

To investigate the adhesion provided by the nanowire structures, nanowire films were pressed onto a vertical glass slide with the nanowire side in contact with the slide. Then, weight was added to the film until it fell off the glass slide. The force used to adhere the film to the slide was varied. The relationship between the force used to adhere the film to the slide and the total force the film could hold up can be seen in Figure 17E. Generally, an increase in the forced used to press the film into the surface led to an increase in the total weight that can be held up. In addition, the nanowire structures greatly increased the total amount of weight that could be held by the film. This can also be seen in the inset of Figure 17E where a 10 mg square of nanowire augmented film, about 5 mm by 5 mm, was able to hold up a 2.3 g American dime. More interestingly, the curling ability of the film can synergize with the increased adhesion and can allow the film to match curved surfaces, thereby increasing the total contact area and adhesive force. As seen in the plot and schematics shown in Figure 17F, when the film is adhered to a curved surface, increasing the temperature of the film allows it to better match the curvature of the surface thus drastically increasing the total weight that can be loaded on the film. This same effect is barely noticeable when the nanowires are removed from the surface of the film. The film is still able to match the curvature of the surface, but without the increased contact area and adhesion from the nanowires, the film is not able to hold significant amounts of weight.

In addition to the increased loaded weight seen when combining the curling and nanowire structures, the films are also able to crawl along the ground like an inchworm.

As seen plotted in Figure 17G and photographed in Figure 17H, when the nanowires are removed from one end of the film, cycling the heat to cause the film to curl and flatten allows the film to slowly crawl along a flat glass slide. The asymmetry of the increased friction caused when one side is stripped of its nanowires causes an imbalance in the forces during curling, where the nanowire side pulls the non-nanowire side, and flattening, where the non-nanowire side acts as an anchor and the nanowire side lifts and reaches out completing the cycle. The curling of the material is even able to lift small amounts of additional weight on the order of the weight of the film. The crawling is stable and could be extended out for long periods of time with subsequent heating and cooling cycles.

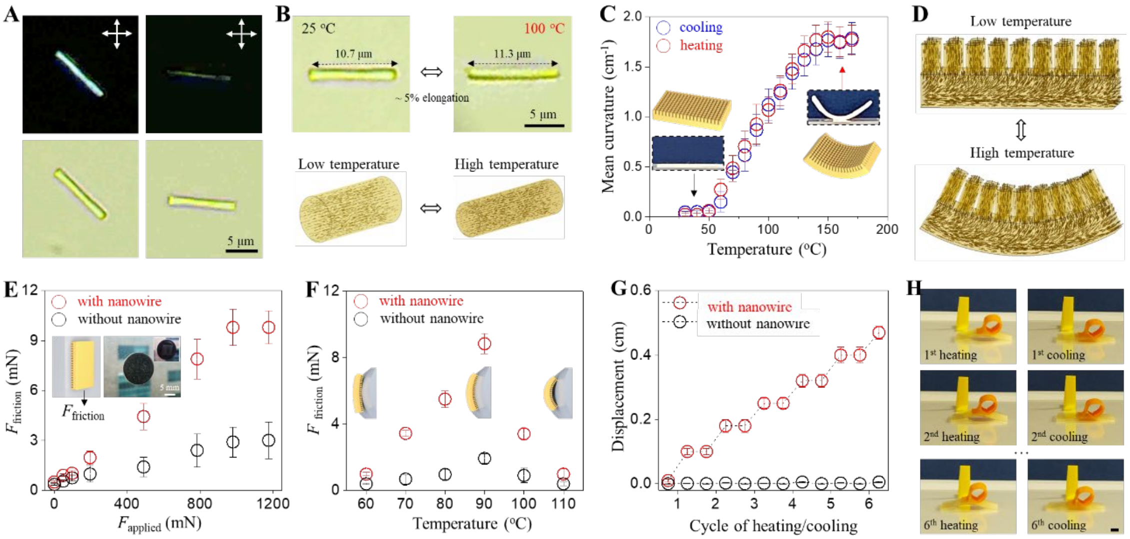

Figure 17. Orientation of LC mesogens and associated temperature dependent macroscopic deformations and increased adhesion of LCE nanowire films.

We hypothesized that the nanowires could also cause irregularities in solvent uptake. Commonly, solvent-induced swelling can cause the stimuli-responsive macroscopic deformations seen in LCEs.[69,143,144] The deformations caused by swelling generally mimic those seen in response to temperature. When exposed to the vapor of an appropriate solvent, such as toluene, the films curl in the direction of the nanowires, just like when heated, schemed in the top part of Figure 18A. However, when exposed to a droplet of toluene, the films curl in the opposite direction, as schemed in the bottom part of Figure 18B. We suspect this is caused by capillary forces gathering the toluene close to the film with the nanowires causing an unequal swelling in the film. This swelling then causes the nanowire side to expand instead of contract, causing the curling to happen in the opposite direction. The film's response over time to both solvent vapor and droplets are shown in Figure 18B. Additionally, increasing the amount of toluene was found to increase the total curvature of the film reaching an eventual maximum curvature at low amounts of solvent, as seen in Figure 18C. Similar to the curling caused by temperature, the curling caused by toluene could also be used synergistically with the increased adhesion of the nanowire structures to match and adhere to curved surfaces, as seen in Figure 18C. This effect was found to only be caused by solvents with an appropriate polarity. A number of different solvents were investigated with the maximum mean curvature seen in Figure 18D. Only toluene was found to cause any significant change to the dimensions of the film.

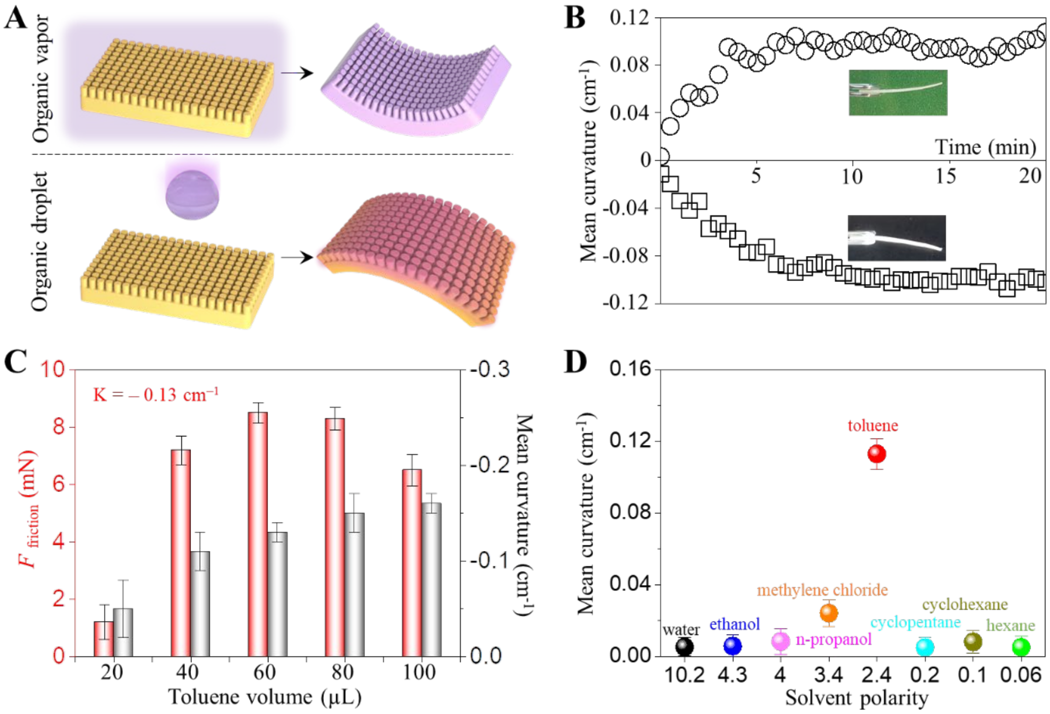

Figure 18. Solvent dependent shape deformations of LCE nanowire films.

3.6 Conclusion

By using anodized aluminum oxide templates with patterned nanovoids, we were able to create liquid crystal elastomer films with nanowires on the surface. These nanoscale surface structures were shown to increase the adhesion to glass substrates that increased with an increase in the force used to press the film to the surface, just like many pressure-sensitive adhesives. These nanowire-augmented liquid crystal elastomers retained their unique stimuli-responsive deformations and were able to curl in response to both a temperature change and the application of a solvent. By synergistically combining the curling deformation with the adhesion amplification of the nanowires, these films were shown to be able to strongly adhere to curved surfaces. The films were also shown to be able to crawl and carry weight across a flat surface by cycling the temperature.

Overall, the results reported here showcase the increase in utility of nanostructure augmented liquid crystal elastomers, expanding the applications of these materials further into soft robotics. The adhesion of the structures synergizes well with the stimuli-responsiveness of the materials unlocking new options and designs. Finally, the opposite deformations afforded by the different application methods of solvents opens up new avenues to match the curvature of a variety of surfaces.

Chapter 4 Anisotropic solvent-aligned polymerization for controlling conformation in amorphous polymers

4.1 Preface

This chapter comes from a manuscript being prepared for submission to *Science* in 2024. It is focused on the creation of liquid crystal elastomer-like materials out of non-liquid crystalline monomers. This expands the monomer selection of reversible deforming materials which allows their application in otherwise untouched areas, such as a plethora of bio-based applications.

4.2 Abstract

Controlling polymer chain conformations is crucial in defining the physicochemical properties of polymers. Aligned chain conformations enhance ion and electron conductivity and enable reversible shape morphing in shape-changing polymers. Although achieved in intrinsically crystalline polymers, aligning chains in intrinsically amorphous polymers is challenging because of a rapid, irreversible relaxation into random coil conformations upon heating and a lack of traditional chemical structures that are required for preserving alignment. To address this challenge, here we develop a revolutionary method, anisotropic solvent-aligned polymerization (ASAP), which involves polymerizing amorphous monomers within a non-reactive nematic liquid crystal (LC) solvent, strategically executed at low temperatures. The LC solvent acts as a soft nanoconfinement, significantly enhancing the alignment of amorphous polymers. Manipulation of

crosslinking density and interactions between the resulting polymer and the solvent during LC extraction enables the kinetic trapping of polymer chains in an aligned configuration post LC removal, thereby enabling reversible shape morphing in amorphous polymers. ASAP can extend to various LC mesophases and amorphous monomers, expanding the application of amorphous polymers in diverse fields such as soft actuators, optics, and polymer-stabilized LCs.

4.3 Introduction

The conformation of polymer chains, or how polymer chains are spatially arranged, is crucial to achieve desired physicochemical properties. The strategic alignment of polymer chains has been shown to enhance mechanical strength,[145,146] elasticity,[147-149] and ion/electron conductivity in polymeric materials,[150,151] In addition, the opportunity for reversible conformational changes, such as transitioning from aligned to random coil conformations, is essential for the design of stimuli-responsive two-way shape memory polymers and is required for their use as artificial muscles and soft robotics.[12,68] Current chain alignment approaches primarily focus on external fields or hard nanoconfinements, including mechanical stretching,[152,153] flow-induced alignment,[154,155] electric/magnetic fields,[6,156] surface-induced alignment,[157,158] and in-situ polymerization within nanopores, such as in anodic aluminum oxide.[4,159] However, these methods mainly achieve polymer chain alignment in polymers with intrinsic crystallinity [e.g., (semi)crystalline,[58,158] liquid crystalline,[93,157] and conjugated polymers[4,6]], presenting a grand challenge for intrinsically amorphous polymers like polymethyl methacrylate (PMMA), polystyrene, and polybutyl acrylate, which lack necessary molecular motifs for self-alignment. Moreover, a rapid and irreversible chain relaxation into a random coil upon heating blocks the creation of a two-way shape memory effect.

In 1969, Pierre-Gilles de Gennes foresaw that the polymerization and crosslinking of intrinsically amorphous polymers in a non-reactive nematic liquid crystal (LC) solvent could imprint the LC ordering into the polymer network (1st prediction).[160] Despite this insightful prediction, previous attempts to polymerize amorphous monomers in non-reactive LC solvents at intermediate and high temperatures have proven insufficient in achieving this critical alignment of polymer chains. As schemed in Figure 19A, high polymerization temperatures cause the LC solvent to remain in the isotropic phase throughout the entire polymerization process, forming LC organogels,[161-163] while intermediate temperatures cause LCs to initially exist in the isotropic phase and then transition into the nematic phase through polymerization-induced phase separation, leading to polymer-dispersed LCs (PDLCs).[164-168] Even when the polymer chains are predicted to be successfully aligned by a nematic LC, the removal of the LC solvent allows the polymers to relax without major obstacle towards the random coil conformation, just as de Gennes further predicted (2nd prediction).[160] To the best of our knowledge, these predictions, and the benefits that the first prediction offers, remain unrealized.

To experimentally address both of de Gennes' predictions, we present a novel approach, anisotropic solvent-aligned polymerization (ASAP), involving the synthesis and alignment of polymer chains by polymerizing and crosslinking amorphous monomers in a non-reactive LC solvent at low temperatures. Distinct from the creation of LC gels and PDLCs, low-temperature polymerization maintains the LC nematic phase throughout the entire process, acting as a soft nanoconfinement and enhancing the alignment of the intrinsically amorphous polymers. More importantly, by manipulating the crosslinking density and extracting the LC using a solvent with appropriate solvent−polymer interactions kinetically traps the polymer chains in the aligned conformation from the polymerization process in nematic LCs. The metastability of this aligned conformation endows the crosslinked amorphous polymers with a remarkable two-way memory effect, facilitating reversible shape deformations. Finally, ASAP introduces intricate alignments in amorphous polymers, broadening their application in soft actuators and robotics, optics, and polymer-stabilized LCs.

4.4 Experimental Section

4.4.1 Materials

E7, which is a mixture of 4-(4-heptylphenyl)benzonitrile (7CB), 4-(4-octoxyphenyl)benzonitrile (8OCB), 4-(4-pentylphenyl)benzonitrile (5CB), and 4-[4-(4-pentylphenyl)phenyl]benzonitrile (5CT), was purchased from Synthon Chemicals Ltd. The following chemicals were purchased from Sigma-Aldrich: 2,2-dimethoxy-2-phenylacetophenone (DMPAP), dimethyloctadecyl [3-(trimethoxysilyl)propyl] ammonium chloride (DMOAP), poly(pyromellitic dianhydride-co-4,4’-oxydianiline) amic acid, 1-methyl-2-pyrrolidinone, Elvamide pellets, methyl methacrylate (MMA), 1,6-Hexanediol diacrylate (HDDA), and ethanol. Plain microscope slides (25 mm × 75 mm × 1 mm) were purchased from Fisher Scientific. Unless stated otherwise, purchased chemicals and materials were used as received without further modification or purification.

4.4.2 Optical Cell Creation

First, uncoated glass microscope slides were washed three times with water and ethanol. Then, they were spin coated with 200 μL of an Elvamide/methanol mixture, created at a ratio of 0.125 g of Elvamide pellets to 100 mL of methanol. The spin coater was set to spin at 2000 rpm for 20 second. Next, the coated glass slides were rubbed with velvet 60 times to create a parallel alignment layer. Two rubbed glass slides were paired together with their rubbing directions going in opposite directions. Spacers were placed between either end of the glass slides and a UV curable adhesive was used to glue the ends of the glass slides together. An offset was left at the side of the glass slides to assist with filling through capillary forces.

4.4.3 Anisotropic Solvent-Aligned Polymerization

A mixture of 87.5 volume% E7, 10 volume% MMA, and 2.5 volume% HDDA was created. An additional 1 weight% of DMPAP photoinitiator was added based on the total weight of the added MMA and HDDA. The mixture was mixed well using a vortex and was injected into the optical cells using capillary forces. Once filled, the cells were left to sit at room temperature for 10 minutes. It should be noted that the liquid crystals were in the isotropic phase at room temperature because of the addition of non-LC molecules. Next, the filled cells were placed on a liquid nitrogen fueled Instec HCP 204S benchtop thermal plate set at -40 °C for 10 minutes. The flow of liquid nitrogen was controlled by an Instec mK2000 temperature control unit and an Instec LN2-P liquid nitrogen pump. This allowed the entirety of the mixture to reach the nematic phase. Next, the thermal plate was raised to -20 °C for 3 minutes to allow the material to more quickly align with the aligning surfaces. The temperature was then brought back down to -40 °C for another 10 minutes before polymerizing with a 365 nm UV lamp that output 10 mW/cm^2 for 15 minutes. The samples were then allowed to return to room temperature, and some were placed in ethanol to remove the liquid crystals.

4.4.4 Deformation Measurements

After LC removal, the formed polymer films were carefully broken out of the optical cells and were cut down to be approximately 10 mm by 4 mm. Next, the films were placed on a hotplate and the temperature was changed. Images were taken of the films at different temperature and were analyzed using a custom MATLAB code that can measure uniaxial and curling deformations.

4.4.5 X-ray Characterization

The orientation of the LC functional groups and aligned polymer chains was determined by wide-angle x-ray scattering (WAXS). A Xenocs Inc. Xeuss 2.0 laboratory beamline system with an x-ray wavelength of 1.54 Å was used. A large vacuum chamber was used to minimize air scattering. Diffraction patterns of the prepared amorphous film samples were recorded using a Pilatus 1M detector (Dectris Inc.) with an exposure time of 1.5 hours and processed using the Nika software package, in combination with WAXSTools wavemetrics Igor. The emitter was 15 cm from the sample.

4.5 Results and Discussion

To test de Gennes' 1st prediction, we investigated the impact of LC mesophase (polymerization temperature) on polymer chain conformations by polymerizing an amorphous monomer and an amorphous crosslinker in a non-reactive, nematic LC solvent, E7 (Figure 19B). E7 was selected in this work as pure E7 exhibits a nematic phase over a wide temperature range (from −62ºC to 60ºC). Hexanediol diacrylate (HDDA) and 2,2-dimethoxy-2-phenylacetophenone (DMPAP) served as the crosslinker and photoinitiator, respectively (Figure 19B). Photopolymerization was carried out by UV radiation at 365 nm, with a reaction vessel constructed from Elvamide-functionalized glass slides promoting a parallel ordering of E7. In the first set of experiments, methyl methacrylate (MMA) was the model amorphous monomer.

When the polymerization was conducted in isotropic E7 at 70ºC [above the nematic−isotropic phase transition temperature ($T_{N–I}$) of pure E7], the E7-infused PMMA film exhibited a dark appearance under a polarized light microscope while still at this elevated temperature. Upon cooling to room temperature, the uniformly dispersed E7 transitioned to the nematic phase, revealing the well-dispersed E7 in the film without macroscopic phase separation (Figure 19C), a characteristic of LC gels. On the other hand, when polymerization was carried out at an intermediate temperature (25ºC), a polymerization-induced phase separation process occurred, resulting in a polydomain morphology in the E7-infused PMMA films at all angles of rotation (Figure 19D), a characteristic of PDLCs.

It is well established that the presence of non-LC species can reduce the $T_{N–I}$ of LCs and induce the coexistence of the isotropic and nematic phases. For instance, the transition temperature between the coexisting isotropic/nematic phase and the uniform nematic phase of a mixture comprising MMA (10%wt), HDDA (2.5%wt), and E7 (87.5%wt) was determined to be around −20ºC using polarized light microscopy. To ensure that the mixture remained in the nematic phase throughout the polymerization process, the polymerization temperature was set at −40ºC. As shown in Figure 19E, in contrast to traditional LC gels or PDLCs, a bright−dark optical transition occurred in low-temperature polymerized systems upon rotation under crossed polarizers. This observation confirms that the presence of nematically ordered LCs during the polymerization of amorphous monomers generates sufficient nanoconfinement to achieve highly aligned conformations. To the best of our knowledge, this provides the first experimental evidence supporting de Gennes' 1st prediction.

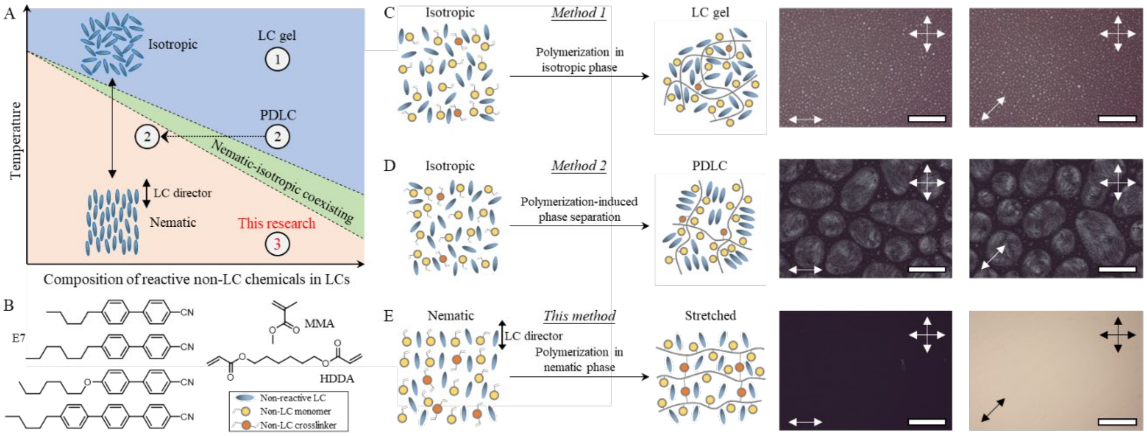

Figure 19. Polymerization of amorphous monomers in LCs to create LC gels, PDLCs, and aligned polymer networks. Scale bars, 200 µm.

To provide insight into de Gennes' 2nd prediction, we used an organic solvent to extract E7 and analyze the chain conformation of the purely crosslinked PMMA network following the evaporation of the extraction solvent, as illustrated in Figure 20A. When using a good solvent for PMMA, such as acetone, the resulting crosslinked PMMA film exhibited a uniform dark appearance under a polarized light microscope. These results suggest a random coil conformation after LC removal, thus confirming de Gennes' 2nd prediction. Similar disordered chain alignment was observed in the PMMA films obtained using Methods 1 and 2 (LC gel and PDLC) after the extraction of E7 (Figure 33 in Appendix C).

However, surprisingly, when a poor solvent for PMMA, such as ethanol, was used, the PMMA network retained its birefringence (Figure 20B) and exhibited anisotropic patterns in the 2D WAXS pattern (Figure 20C). Work is currently ongoing to further characterize the suspected alignment through differential scanning calorimetry, scanning electron microscopy, and infrared transition moment orientational analysis. These findings suggest that the crosslinked polymer chains undergo alignment templated by E7 during the polymerization process, and remarkably, this alignment persists even after the removal of E7, contradicting de Gennes' 2nd prediction.

We attribute the cause of this 'contradiction' to the solvent−polymer interactions during the LC removal process. When using poor solvents for LC removal, the preferred polymer−polymer self-interactions do not provide necessary free volume needed for the polymer chains to relax towards a random coil conformation, which is the most thermodynamically stable chain conformation for intrinsically amorphous polymers. Consequently, the aligned polymer chains experience shrinkage during LC removal, resulting in the kinetic trapping of the aligned conformation even after the removal of the LCs. Even with this shrinkage, however, we can confirm that the ethanol successfully removed all of the E7, as seen in the ATR-FTIR data in Figure 34 of Appendix C. In contrast, if a good solvent is used to remove the LCs, the preferred solvent−polymer interactions give rise to significant swelling. This swelling allows the polymer chains to reorganize into random coil conformations, aligning with de Gennes' 2nd prediction.

Considering that the equilibrium state of the intrinsically amorphous polymers is a random coil, we aimed to manipulate the shape memory effect by leveraging the metastability of the kinetically trapped aligned chain conformation. Below a threshold temperature which is likely the glass transition temperature of the crosslinked PMMA film, the aligned polymer chains can undergo reversible relaxation and alignment in response to temperature variations, resulting in a two-way shape memory effect similar to LCEs, as illustrated in Figure 20D. As demonstrated in Figure 20E, after ASAP and removing E7 using ethanol, the resulting crosslinked PMMA films exhibit a reversible unidirectional elongation in the direction of the E7 orientation during polymerization with an actuation temperature window between 80−90ºC. This shape deformation is repeatable for at least 1,000 cycles (Figure 20F). However, above the suspected glass transition temperature, an irreversible chain conformational change occurs, wherein the aligned polymer chains irreversibly reorganize towards the random coil conformation and cannot recover the aligned state even after cooling. As a result, the polymer networks are not capable of reversible conformational transitions and shape deformations, leading to a one-way shape memory effect, as evidenced in Figure 20G.

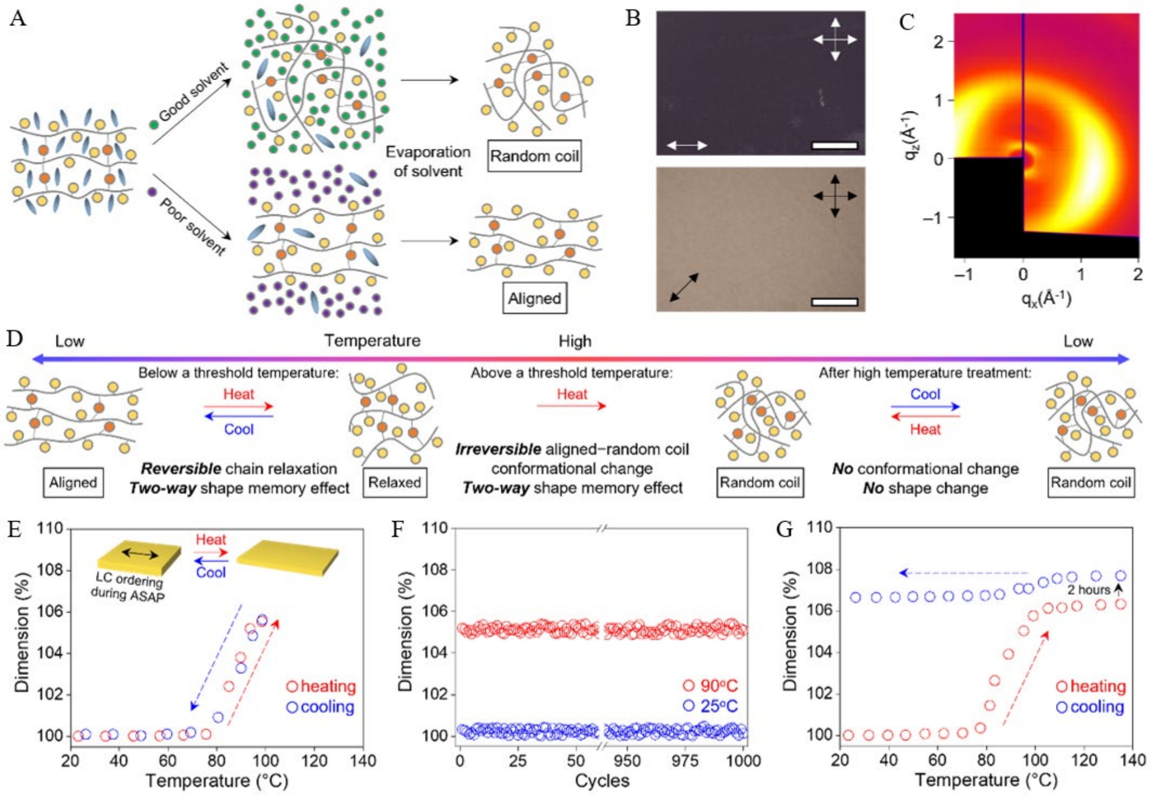

Figure 20. Effect of solvent during removal and two-way shape memory effect of polymer films created through ASAP.

To provide a complete view of ASAP materials, we present a summary of the effect of crosslinking density on the chain conformations of polymer networks synthesized in LCs, as shown in Figure 21. A lower threshold of crosslinking density is necessary to retain the chain alignment imprinted by the nematic LCs during ASAP, given the intrinsic lack of crystallinity in amorphous polymers. Insufficient crosslinking densities cause the polymer chains to lose their aligned conformations, reverting to random coils and separating from the bulk LC. Additionally, a second, higher threshold of crosslinking density exists. Beyond this threshold, aligned polymer chain conformations can be maintained after LC removal, but limited free volume may impede reconfiguration upon heating. This highly crosslinked polymer network demonstrates high thermal stability, limiting significant conformational changes and macroscopic shape deformation, akin to the characteristics of liquid crystal networks (LCNs).

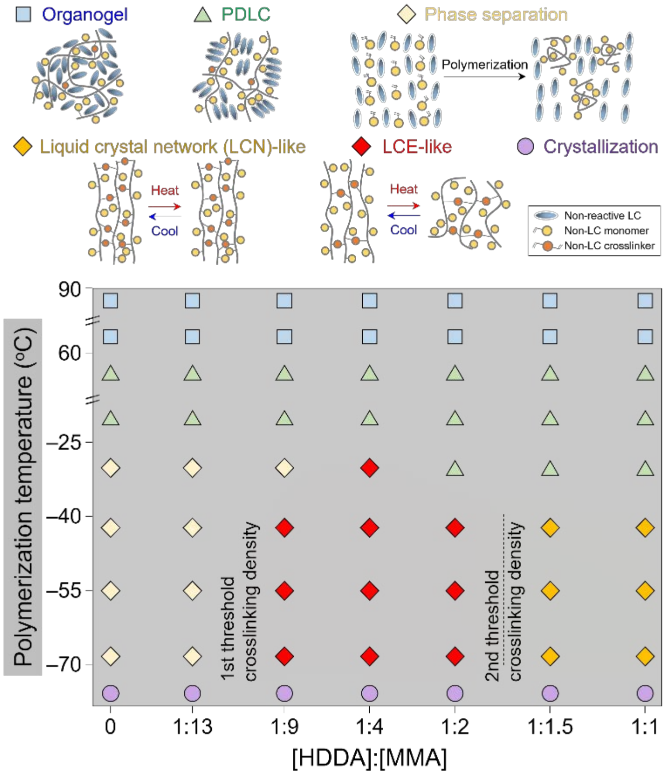

Figure 21. Design space for materials polymerized in LCs using ASAP.

Finally, we demonstrate the generalizability of ASAP to a variety of amorphous monomers. Beyond MMA, ASAP can effectively align polymer networks using a wide range of amorphous monomers, including styrene, methyl acrylate, n-butyl acrylate and t-butyl acrylate, as evident in Figure 22. We note here that the crosslinked polymer networks formed by different monomers exhibited unique actuation temperatures, indicating varying chain rigidity and the ability of the polymers to relax towards random coil conformations.

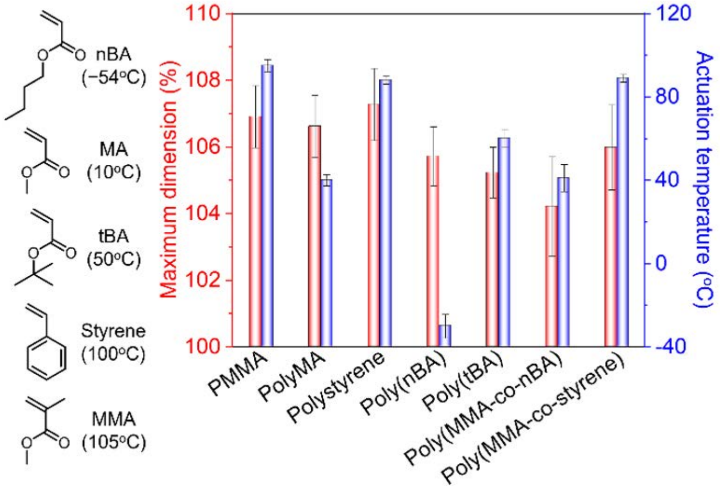

Figure 22. Generalizability of the ASAP method to a variety of different amorphous monomers.

4.6 Conclusion

In conclusion, our work fulfills de Gennes' predictions regarding the alignment of polymer chains through our ASAP approach. This innovative method utilizes polymerization in a non-reactive nematic LC solvent at low temperatures, achieving controlled alignment in intrinsically amorphous polymers. Remarkably, this alignment can be kinetically preserved even after LC removal through proper crosslinking and careful LC extraction, laying the foundation for controlling chain conformations in intrinsically amorphous polymers. Consequently, the materials can switch between a one-way and two-way shape memory effect by careful control of the temperature. The versatility of ASAP extends to a variety of LC mesophases and amorphous polymers, allowing for significant adjustments in shape actuation temperatures.

Overall, ASAP successfully overcomes challenges posed by the chemical structure of intrinsically amorphous polymers, expanding their application in diverse fields, from soft actuators and robotics to optics and polymer-stabilized LCs. Future efforts will aim to leverage ASAP for aligning chains of polymer electrolytes with enhanced directional lithium-ion conductivity and optimizing the conformation of inherently disordered conducting polymers for improved charge carrier mobility.

Chapter 5 Conclusions and Future Work

For the first thrust, copolymerizing different configurations of liquid crystal monomers provided a new avenue to tune the magnitude and direction of the deformation. It also elucidated the negative interactions between different configurations caused by their inability to properly align along the backbone. The copolymerization method used in this thrust is not only easily integrated into existing alignment technologies, such as 3D printing and photoalignment, but it also serves as an easier way to create more complex deformations through patterning the composition along the material instead of the alignment structure. Future work in this area involves investigating different copolymerization structures, such as block and gradient, and different architectures, such as cyclic and bottlebrush. These different structure and architectures are hypothesized to produce unique deformations that can be used for new applications. Other future work would include an investigation into the use of other liquid crystal monomers.

In the second thrust, the addition of nanoscopic surface structures increased the adhesion of the films to surfaces. This increased adhesion can be synergistically combined with the deformation of the films to match and adhere well to curved surfaces. Additionally, the unique interactions with solvents provided by the surface structures opens up potential new ways to design sensors. Future work for this thrust includes using other types of liquid crystal monomers, including mixtures provided by the results of the first thrust, as well as an investigation into underwater applications to pin and move oily droplets for underwater droplet reactor design.

With the third and final main thrust, liquid crystals were successfully used to template their ordering onto the polymer chains of intrinsically amorphous polymers, such as poly(methyl methacrylate) and polystyrene, which experimentally proves predictions made many years ago by a founding member of the liquid crystal elastomer field. This has allowed for new designs that are better suited for biomedical applications, as these intrinsically amorphous polymers have already seen heavy use in some biomedical applications. It was found that this imprinted ordering enables the amorphous polymer systems to deform in response to an external stimulus just like traditional liquid crystal elastomers. It was determined that the alignment is only kinetically trapped and can be nullified through swelling with a solvent or through high temperature melting. Future work for this thrust can go in many new directions, including investigating more complex alignments and alignment methods already used with liquid crystal elastomers. For example, it is hypothesized that the helical twist provided by chiral liquid crystals can be imprinted into the polymer network thus creating novel materials for optics applications. Likewise, using complex photoalignment methods, complex shapes and deformations can be created, such as arrays of cones or birefringent images in a film. Finally, the most exciting future path with this thrust is focused on the upcycling of plastic waste into usable, high value materials through chemical depolymerization and liquid crystal templated polymerization.

Overall, by completing these three thrusts, I have expanded the utility of liquid crystal elastomers and have opened the design space to include non-traditional monomers. This work will increase their use in soft robotics, actuators, and sensors, areas where they already see heavy use. In addition, this work opens them up to new biomedical applications by overcoming the inherent challenges with liquid crystals, specifically their cost, difficult synthesis, and hazardous nature.

References

1 Guo, X., Baumgarten, M. & Müllen, K. Designing π-conjugated polymers for organic electronics. *Progress in Polymer Science* **38**, 1832-1908 (2013).

2 Kertesz, M., Choi, C. H. & Yang, S. Conjugated polymers and aromaticity. *Chemical reviews* **105**, 3448-3481 (2005).

3 Koßmehl, G. Semiconductive conjugated polymers. *Berichte der Bunsengesellschaft für physikalische Chemie* **83**, 417-426 (1979).

4 Lo, K. H. *et al.* Induced chain alignment of conjugated polymers within nanoporous template. *Advanced Functional Materials* **21**, 2729-2736 (2011).

5 Qiu, Z., Hammer, B. A. & Müllen, K. Conjugated polymers–Problems and promises. *Progress in Polymer Science* **100**, 101179 (2020).

6 Xi, Y. & Pozzo, L. D. Electric field directed formation of aligned conjugated polymer fibers. *Soft Matter* **13**, 3894-3908 (2017).

7 Chatterjee, S. & Chi-Leung Hui, P. Review of Stimuli-Responsive Polymers in Drug Delivery and Textile Application. *Molecules* **24** (2019). https://doi.org:10.3390/molecules24142547

8 Bajpai, A. K., Shukla, S. K., Bhanu, S. & Kankane, S. Responsive polymers in controlled drug delivery. *Progress in Polymer Science* **33**, 1088-1118 (2008). https://doi.org:https://doi.org/10.1016/j.progpolymsci.2008.07.005

9 Schmaljohann, D. Thermo- and pH-responsive polymers in drug delivery. *Advanced Drug Delivery Reviews* **58**, 1655-1670 (2006). https://doi.org:https://doi.org/10.1016/j.addr.2006.09.020

10 Zhao, Y. *et al.* Stimuli-Responsive Polymers for Soft Robotics. *Annual Review of Control, Robotics, and Autonomous Systems* **5**, 515-545 (2022). https://doi.org:10.1146/annurev-control-042920-014327

11 Shen, Z., Chen, F., Zhu, X., Yong, K.-T. & Gu, G. Stimuli-responsive functional materials for soft robotics. *Journal of Materials Chemistry B* **8**, 8972-8991 (2020). https://doi.org:10.1039/D0TB01585G

12 Koshima, H. *Mechanically Responsive Materials for Soft Robotics*. (Wiley, 2019).

13 Kim, S. W., Bae, Y. H. & Okano, T. Hydrogels: Swelling, Drug Loading, and Release. *Pharmaceutical Research* **9**, 283-290 (1992). https://doi.org:10.1023/A:1015887213431

14 Preller, T. *et al.* Particle-reinforced and functionalized hydrogels for SpineMan, a soft robotics application. *Journal of Materials Science* **54**, 4444-4456 (2019). https://doi.org:10.1007/s10853-018-3106-6

15 Deng, C. *et al.* Amoeboid soft robot based on multi-material composite 3D printing technology. *Journal of Magnetism and Magnetic Materials* **588**, 171390 (2023). https://doi.org:https://doi.org/10.1016/j.jmmm.2023.171390

16 Hao, J. & Weiss, R. A. Mechanically Tough, Thermally Activated Shape Memory Hydrogels. *ACS Macro Letters* **2**, 86-89 (2013). https://doi.org:10.1021/mz3006389

17 Lendlein, A. & Kelch, S. Shape-memory polymers. *Angewandte Chemie International Edition* **41**, 2034-2057 (2002).

18 Azadi, F. *et al.* Influence of graphene oxide on thermally induced shape memory behavior of PLA/TPU blends: correlation with morphology, creep behavior, crystallinity, and dynamic mechanical properties. *Macromolecular Materials and Engineering* **306**, 2000576 (2021).

19 Behl, M. & Lendlein, A. Triple-shape polymers. *Journal of Materials Chemistry* **20**, 3335-3345 (2010).

20 Bellin, I., Kelch, S., Langer, R. & Lendlein, A. Polymeric triple-shape materials. *Proceedings of the National Academy of Sciences* **103**, 18043-18047 (2006).

21 Wang, Z. *et al.* Dually actuated triple shape memory polymers of cross-linked polycyclooctene–carbon nanotube/polyethylene nanocomposites. *ACS applied materials & interfaces* **6**, 20051-20059 (2014).

22 Anderson, I. A., Gisby, T. A., McKay, T. G., O'Brien, B. M. & Calius, E. P. Multi-functional dielectric elastomer artificial muscles for soft and smart machines. *Journal of applied physics* **112** (2012).

23 Brochu, P. & Pei, Q. Dielectric elastomers for actuators and artificial muscles. *Electroactivity in polymeric materials*, 1-56 (2012).

24 O'Halloran, A., O'malley, F. & McHugh, P. A review on dielectric elastomer actuators, technology, applications, and challenges. *Journal of Applied Physics* **104** (2008).

25 Suo, Z. Theory of dielectric elastomers. *Acta Mechanica Solida Sinica* **23**, 549-578 (2010).

26 Liu, D. & Broer, D. J. Liquid crystal polymer networks: preparation, properties, and applications of films with patterned molecular alignment. *Langmuir* **30**, 13499-13509 (2014).

27 White, T. J. & Broer, D. J. Programmable and adaptive mechanics with liquid crystal polymer networks and elastomers. *Nature materials* **14**, 1087-1098 (2015). https://doi.org:10.1038/nmat4433

28 Ware, T. H., McConney, M. E., Wie, J. J., Tondiglia, V. P. & White, T. J. Voxelated liquid crystal elastomers. *Science* **347**, 982-984 (2015).

29 Buguin, A., Li, M.-H., Silberzan, P., Ladoux, B. & Keller, P. Micro-actuators: When artificial muscles made of nematic liquid crystal elastomers meet soft lithography. *Journal of the American Chemical Society* **128**, 1088-1089 (2006).

30 Li, C. *et al.* Light-controlled quick switch of adhesion on a micro-arrayed liquid crystal polymer superhydrophobic film. *Soft Matter* **8**, 3730-3733 (2012).

31 Zhang, J. *et al.* Liquid crystal elastomer-based magnetic composite films for reconfigurable shape-morphing soft miniature machines. *Advanced Materials* **33**, 2006191 (2021).

32 Barnes, M. *et al.* Reactive 3D printing of shape-programmable liquid crystal elastomer actuators. *ACS applied materials & interfaces* **12**, 28692-28699 (2020).

33 Davidson, E. C., Kotikian, A., Li, S., Aizenberg, J. & Lewis, J. A. 3D printable and reconfigurable liquid crystal elastomers with light-induced shape memory via dynamic bond exchange. *Advanced Materials* **32**, 1905682 (2020).

34 Kotikian, A., Truby, R. L., Boley, J. W., White, T. J. & Lewis, J. A. 3D printing of liquid crystal elastomeric actuators with spatially programed nematic order. *Advanced materials* **30**, 1706164 (2018).

35 Autumn, K. *et al.* Adhesive force of a single gecko foot-hair. *Nature* **405**, 681-685 (2000).

36 Autumn, K. *et al.* Evidence for van der Waals adhesion in gecko setae. *Proceedings of the National Academy of Sciences* **99**, 12252-12256 (2002).

37 Jang, K. I. *et al.* Soft network composite materials with deterministic and bio-inspired designs. *Nat Commun* **6**, 6566 (2015). https://doi.org:10.1038/ncomms7566

38 Xia, F. & Jiang, L. Bio-inspired, smart, multiscale interfacial materials. *Advanced materials* **20**, 2842-2858 (2008).

39 Qin, H. & Mather, P. T. Combined one-way and two-way shape memory in a glass-forming nematic network. *Macromolecules* **42**, 273-280 (2009).

40 Klein, Y., Efrati, E. & Sharon, E. Shaping of elastic sheets by prescription of non-Euclidean metrics. *Science* **315**, 1116-1120 (2007).

41 Lyon, G. B. *et al.* Remoldable thiol–ene vitrimers for photopatterning and nanoimprint lithography. *Macromolecules* **49**, 8905-8913 (2016).

42 Schaffner, M. *et al.* 3D printing of robotic soft actuators with programmable bioinspired architectures. *Nature communications* **9**, 878 (2018).

43 Le Ferrand, H., Bouville, F., Niebel, T. P. & Studart, A. R. Magnetically assisted slip casting of bioinspired heterogeneous composites. *Nature materials* **14**, 1172-1179 (2015).

44 Zhao, Q., Qi, H. J. & Xie, T. Recent progress in shape memory polymer: New behavior, enabling materials, and mechanistic understanding. *Progress in Polymer Science* **49**, 79-120 (2015).

45 Jin, B. *et al.* Programming a crystalline shape memory polymer network with thermo-and photo-reversible bonds toward a single-component soft robot. *Science advances* **4**, eaao3865 (2018).

46 Zou, W. *et al.* Light-triggered topological programmability in a dynamic covalent polymer network. *Science Advances* **6**, eaaz2362 (2020).

47 Hu, W., Lum, G. Z., Mastrangeli, M. & Sitti, M. Small-scale soft-bodied robot with multimodal locomotion. *Nature* **554**, 81-85 (2018).

48 Capadona, J. R., Shanmuganathan, K., Tyler, D. J., Rowan, S. J. & Weder, C. Stimuli-responsive polymer nanocomposites inspired by the sea cucumber dermis. *science* **319**, 1370-1374 (2008).

49 Zarzar, L. D. & Aizenberg, J. Stimuli-responsive chemomechanical actuation: A hybrid materials approach. *Accounts of chemical research* **47**, 530-539 (2014).

50 Fratzl, P. & Barth, F. G. Biomaterial systems for mechanosensing and actuation. *Nature* **462**, 442-448 (2009).

51 Erb, R. M., Sander, J. S., Grisch, R. & Studart, A. R. Self-shaping composites with programmable bioinspired microstructures. *Nature communications* **4**, 1712 (2013).

52 Sano, K., Ishida, Y. & Aida, T. Synthesis of anisotropic hydrogels and their applications. *Angewandte Chemie International Edition* **57**, 2532-2543 (2018).

53 Sydney Gladman, A., Matsumoto, E. A., Nuzzo, R. G., Mahadevan, L. & Lewis, J. A. Biomimetic 4D printing. *Nature materials* **15**, 413-418 (2016).

54 Kim, Y. S. *et al.* Thermoresponsive actuation enabled by permittivity switching in an electrostatically anisotropic hydrogel. *Nature materials* **14**, 1002-1007 (2015).

55 Jeon, S.-J., Hauser, A. W. & Hayward, R. C. Shape-morphing materials from stimuli-responsive hydrogel hybrids. *Accounts of chemical research* **50**, 161-169 (2017).

56 Wu, Z. L. *et al.* Three-dimensional shape transformations of hydrogel sheets induced by small-scale modulation of internal stresses. *Nature communications* **4**, 1586 (2013).

57 Xu, B. B., Liu, Q., Suo, Z. & Hayward, R. C. Reversible electrochemically triggered delamination blistering of hydrogel films on micropatterned electrodes. *Advanced Functional Materials* **26**, 3218-3225 (2016).

58 Gao, Y., Liu, W. & Zhu, S. Reversible shape memory polymer from semicrystalline poly (ethylene-co-vinyl acetate) with dynamic covalent polymer networks. *Macromolecules* **51**, 8956-8963 (2018).

59 Pelrine, R., Kornbluh, R., Pei, Q. & Joseph, J. High-speed electrically actuated elastomers with strain greater than 100%. *Science* **287**, 836-839 (2000).

60 Pelrine, R. E., Kornbluh, R. D. & Joseph, J. P. Electrostriction of polymer dielectrics with compliant electrodes as a means of actuation. *Sensors and Actuators A: Physical* **64**, 77-85 (1998).

61 Warner, M. & Terentjev, E. M. *Liquid crystal elastomers*. Vol. 120 (Oxford university press, 2007).

62 Küpfer, J. & Finkelmann, H. Nematic liquid single crystal elastomers. *Die Makromolekulare Chemie, Rapid Communications* **12**, 717-726 (1991).

63 Ohm, C., Brehmer, M. & Zentel, R. Liquid crystalline elastomers as actuators and sensors. *Advanced materials* **22**, 3366-3387 (2010).

64 Lyu, X. *et al.* Liquid crystalline polymers: Discovery, development, and the future. *Polymer* **202**, 122740 (2020).

65 Xiao, Y.-Y., Jiang, Z.-C., Hou, J.-B. & Zhao, Y. Desynchronized liquid crystalline network actuators with deformation reversal capability. *Nature communications* **12**, 624 (2021).

66 Hebner, T. S., Bowman, C. N. & White, T. J. Influence of orientational genesis on the actuation of monodomain liquid crystalline elastomers. *Macromolecules* **54**, 4023-4029 (2021).

67 Wen, Z. *et al.* Reconfigurable LC elastomers: Using a thermally programmable monodomain to access two-way free-standing multiple shape memory polymers. *Macromolecules* **51**, 5812-5819 (2018).

68 Kotikian, A. *et al.* Untethered soft robotic matter with passive control of shape morphing and propulsion. *Science robotics* **4**, eaax7044 (2019).

69 Shang, Y. *et al.* Reversible solvent-sensitive actuator with continuous bending/debending process from liquid crystal elastomer-colloidal material. *Soft Matter* **14**, 5547-5553 (2018).

70 Iamsaard, S. *et al.* Conversion of light into macroscopic helical motion. *Nature chemistry* **6**, 229-235 (2014).

71 Kuenstler, A. S., Kim, H. & Hayward, R. C. Liquid crystal elastomer waveguide actuators. *Advanced Materials* **31**, 1901216 (2019).

72 Zeng, H., Wani, O. M., Wasylczyk, P., Kaczmarek, R. & Priimagi, A. Self-regulating iris based on light-actuated liquid crystal elastomer. *Advanced materials* **29**, 1701814 (2017).

73 Ikeda, T., Mamiya, J. i. & Yu, Y. Photomechanics of liquid-crystalline elastomers and other polymers. *Angewandte Chemie International Edition* **46**, 506-528 (2007).

74 Shin, J. *et al.* Thermally functional liquid crystal networks by magnetic field driven molecular orientation. *ACS Macro Letters* **5**, 955-960 (2016).

75 Na, Y. H., Aburaya, Y., Orihara, H. & Hiraoka, K. Measurement of electrically induced shear strain in a chiral smectic liquid-crystal elastomer. *Physical Review E* **83**, 061709 (2011).

76 Woltman, S. J., Jay, G. D. & Crawford, G. P. Liquid-crystal materials find a new order in biomedical applications. *Nature materials* **6**, 929-938 (2007).

77 Lagerwall, J. P. *et al.* Cellulose nanocrystal-based materials: from liquid crystal self-assembly and glass formation to multifunctional thin films. *NPG Asia Materials* **6**, e80-e80 (2014).

78 Koçer, G. *et al.* Light-Responsive Hierarchically Structured Liquid Crystal Polymer Networks for Harnessing Cell Adhesion and Migration. *Advanced materials* **29**, 1606407 (2017).

79 Gao, Y. *et al.* Biocompatible 3D liquid crystal elastomer cell scaffolds and foams with primary and secondary porous architecture. *ACS Macro Letters* **5**, 4-9 (2016).

80 Bera, T. *et al.* Liquid crystal elastomer microspheres as three-dimensional cell scaffolds supporting the attachment and proliferation of myoblasts. *ACS Applied Materials & Interfaces* **7**, 14528-14535 (2015).

81 Turiv, T. *et al.* Topology control of human fibroblast cells monolayer by liquid crystal elastomer. *Science Advances* **6**, eaaz6485 (2020).

82 Cui, J. *et al.* Bioinspired actuated adhesive patterns of liquid crystalline elastomers. *Advanced Materials* **24**, 4601-4604 (2012).

83 de Haan, L. T. *et al.* Accordion-like actuators of multiple 3D patterned liquid crystal polymer films. *Advanced Functional Materials* **24**, 1251-1258 (2014).

84 Lv, J.-a. *et al.* Photocontrol of fluid slugs in liquid crystal polymer microactuators. *Nature* **537**, 179-184 (2016).

85 Thomsen, D. L. *et al.* Liquid crystal elastomers with mechanical properties of a muscle. *Macromolecules* **34**, 5868-5875 (2001).

86 Shahsavan, H., Salili, S. M., Jákli, A. & Zhao, B. Thermally active liquid crystal network gripper mimicking the self-peeling of gecko toe pads. *Adv. Mater* **29**, 1604021 (2017).
87 Krause, S. *et al.* Nematic main-chain elastomers: Coupling and orientational behavior. *Comptes Rendus. Chimie* **12**, 85-104 (2009).
88 Yao, Y. *et al.* Multiresponsive polymeric microstructures with encoded predetermined and self-regulated deformability. *Proceedings of the National Academy of Sciences* **115**, 12950-12955 (2018).
89 Palagi, S. *et al.* Structured light enables biomimetic swimming and versatile locomotion of photoresponsive soft microrobots. *Nature materials* **15**, 647-653 (2016).
90 Fleischmann, E.-K. *et al.* One-piece micropumps from liquid crystalline core-shell particles. *Nature communications* **3**, 1178 (2012).
91 Pei, Z. *et al.* Mouldable liquid-crystalline elastomer actuators with exchangeable covalent bonds. *Nature materials* **13**, 36-41 (2014).
92 Waters, J. T. *et al.* Twist again: Dynamically and reversibly controllable chirality in liquid crystalline elastomer microposts. *Science advances* **6**, eaay5349 (2020).
93 Kularatne, R. S., Kim, H., Boothby, J. M. & Ware, T. H. Liquid crystal elastomer actuators: Synthesis, alignment, and applications. *Journal of Polymer Science Part B: Polymer Physics* **55**, 395-411 (2017).
94 Broer, D. J., Bastiaansen, C. M., Debije, M. G. & Schenning, A. P. Functional Organic Materials Based on Polymerized Liquid-Crystal Monomers: Supramolecular Hydrogen-Bonded Systems. *Angewandte Chemie International Edition* **51**, 7102-7109 (2012).
95 Wu, Y. *et al.* Controlled orientation of liquid-crystalline polythiophene semiconductors for high-performance organic thin-film transistors. *Applied Physics Letters* **86** (2005).
96 Zhang, Y. *et al.* Seamless multimaterial 3D liquid-crystalline elastomer actuators for next-generation entirely soft robots. *Science advances* **6**, eaay8606 (2020).
97 Traugutt, N. A. *et al.* Liquid-crystal-elastomer-based dissipative structures by digital light processing 3D printing. *Advanced Materials* **32**, 2000797 (2020).
98 Liu, X. *et al.* Reversible and rapid laser actuation of liquid crystalline elastomer micropillars with inclusion of gold nanoparticles. *Advanced Functional Materials* **25**, 3022-3032 (2015).
99 Torras, N., Zinoviev, K. E., Esteve, J. & Sánchez-Ferrer, A. Liquid-crystalline elastomer micropillar array for haptic actuation. *Journal of Materials Chemistry C* **1**, 5183-5190 (2013).
100 Wu, Z. L. *et al.* Microstructured nematic liquid crystalline elastomer surfaces with switchable wetting properties. *Advanced Functional Materials* **23**, 3070-3076 (2013).
101 Gelebart, A. H. *et al.* Making waves in a photoactive polymer film. *Nature* **546**, 632-636 (2017). https://doi.org:10.1038/nature22987
102 Li, C., Liu, Y., Huang, X. & Jiang, H. Direct Sun-Driven Artificial Heliotropism for Solar Energy Harvesting Based on a Photo-Thermomechanical Liquid-Crystal

Elastomer Nanocomposite. *Advanced Functional Materials* **22**, 5166-5174 (2012). https://doi.org:10.1002/adfm.201202038

103 McConney, M. E. *et al.* Topography from topology: photoinduced surface features generated in liquid crystal polymer networks. *Adv Mater* **25**, 5880-5885 (2013). https://doi.org:10.1002/adma.201301891

104 van der Kooij, H. M. *et al.* Morphing of liquid crystal surfaces by emergent collectivity. *Nat Commun* **10**, 3501 (2019). https://doi.org:10.1038/s41467-019-11501-5

105 Liu, D. & Broer, D. J. Self-assembled Dynamic 3D Fingerprints in Liquid-Crystal Coatings Towards Controllable Friction and Adhesion. *Angewandte Chemie International Edition* **53**, 4542-4546 (2014). https://doi.org:10.1002/anie.201400370

106 Visschers, F. L. L., Hendrikx, M., Zhan, Y. & Liu, D. Liquid crystal polymers with motile surfaces. *Soft matter* **14**, 4898-4912 (2018). https://doi.org:10.1039/c8sm00524a

107 Li, S. *et al.* Liquid-induced topological transformations of cellular microstructures. *Nature : International weekly journal of science* **592**, 386-391 (2021). https://doi.org:10.1038/s41586-021-03404-7

108 Wang, X., Luo, Y., Li, B. & Zhu, S. Ab Initio Batch Emulsion RAFT Polymerization of Styrene Mediated by Poly(acrylic acid-b-styrene) Trithiocarbonate. *Macromolecules* **42**, 6414-6421 (2009). https://doi.org:10.1021/ma9010999

109 Sun, X. *et al.* Programmed Synthesis of Copolymer with Controlled Chain Composition Distribution via Semibatch RAFT Copolymerization. *Macromolecules* **40**, 849-859 (2007). https://doi.org:10.1021/ma061677v

110 Chiefari, J. *et al.* Living Free-Radical Polymerization by Reversible Addition−Fragmentation Chain Transfer: The RAFT Process. *Macromolecules* **31**, 5559-5562 (1998). https://doi.org:10.1021/ma9804951

111 Penzel, E., Rieger, J. & Schneider, H. A. The glass transition temperature of random copolymers: 1. Experimental data and the Gordon-Taylor equation. *Polymer* **38**, 325-337 (1997). https://doi.org:10.1016/S0032-3861(96)00521-6

112 Schneider, H. A., Rieger, J. & Penzel, E. The glass transition temperature of random copolymers: 2. Extension of the Gordon-Taylor equation for asymmetric Tg vs composition curves. *Polymer* **38**, 1323-1337 (1997). https://doi.org:https://doi.org/10.1016/S0032-3861(96)00652-0

113 Traugutt, N. A. *et al.* Liquid-crystal order during synthesis affects main-chain liquid-crystal elastomer behavior. *Soft Matter* **13**, 7013-7025 (2017). https://doi.org:10.1039/c7sm01405h

114 Saed, M. O. *et al.* High strain actuation liquid crystal elastomers via modulation of mesophase structure. *Soft matter* **13**, 7537-7547 (2017). https://doi.org:10.1039/c7sm01380a

115 Babakhanova, G. *et al.* Liquid crystal elastomer coatings with programmed response of surface profile. *Nature communications* **9**, 456 (2018). https://doi.org:10.1038/s41467-018-02895-9

116 Hu, J. *et al.* Programmable 3D Shape-Change Liquid Crystalline Elastomer Based on a Vertically Aligned Monodomain with Cross-link Gradient. *ACS applied materials & interfaces* **11**, 48393-48401 (2019). https://doi.org:10.1021/acsami.9b17393

117 Wang, Q. *et al.* Liquid Crystal Elastomer Actuators from Anisotropic Porous Polymer Template. *Macromolecular Rapid Communications* **38** (2017). https://doi.org:10.1002/marc.201600699

118 Han, K., Park, T. Y., Yong, K. & Cha, H. J. Combinational biomimicking of lotus leaf, mussel, and sandcastle worm for robust superhydrophobic surfaces with biomedical multifunctionality: antithrombotic, antibiofouling, and tissue closure capabilities. *ACS applied materials & interfaces* **11**, 9777-9785 (2019).

119 Li, Z. & Guo, Z. Bioinspired surfaces with wettability for antifouling application. *Nanoscale* **11**, 22636-22663 (2019).

120 Liang, Y. *et al.* Lotus leaf-like SiO2 nanofiber coating on polyvinylidene fluoride nanofiber membrane for water-in-oil emulsion separation and antifouling enhancement. *Chemical Engineering Journal* **452**, 139710 (2023).

121 Du Clos, K. T. *et al.* Passive bristling of mako shark scales in reversing flows. *Journal of The Royal Society Interface* **15**, 20180473 (2018).

122 Lang, A. W. *et al.* Movable shark scales act as a passive dynamic micro-roughness to control flow separation. *Bioinspiration & biomimetics* **9**, 036017 (2014).

123 Maderson, P. Keratinized epidermal derivatives as an aid to climbing in gekkonid lizards. *Nature* **203**, 780-781 (1964).

124 Geim, A. K. *et al.* Microfabricated adhesive mimicking gecko foot-hair. *Nature materials* **2**, 461-463 (2003).

125 Jin, K. *et al.* Biomimetic bidirectional switchable adhesive inspired by the gecko. *Advanced Functional Materials* **24**, 574-579 (2014).

126 Shahsavan, H., Salili, S. M., Jákli, A. & Zhao, B. Thermally active liquid crystal network gripper mimicking the self-peeling of gecko toe pads. *Advanced Materials* **29**, 1604021 (2017).

127 Yu, J. *et al.* Gecko-inspired dry adhesive for robotic applications. *Advanced Functional Materials* **21**, 3010-3018 (2011).

128 Ge, L., Sethi, S., Ci, L., Ajayan, P. M. & Dhinojwala, A. Carbon nanotube-based synthetic gecko tapes. *Proceedings of the National Academy of Sciences* **104**, 10792-10795 (2007).

129 Hager, M. D., Bode, S., Weber, C. & Schubert, U. S. Shape memory polymers: Past, present and future developments. *Progress in Polymer Science* **49**, 3-33 (2015).

130 Liu, C., Qin, H. & Mather, P. Review of progress in shape-memory polymers. *Journal of materials chemistry* **17**, 1543-1558 (2007).

131 Ahmad, M. *et al.* Synthesis and characterization of polyurethane-based shape-memory polymers for tailored Tg around body temperature for medical applications. *Macromolecular Chemistry and Physics* **212**, 592-602 (2011).

132 Wang, Y., Li, Y., Luo, Y., Huang, M. & Liang, Z. Synthesis and characterization of a novel biodegradable thermoplastic shape memory polymer. *Materials letters* **63**, 347-349 (2009).

133 Rabani, G., Luftmann, H. & Kraft, A. Synthesis and characterization of two shape-memory polymers containing short aramid hard segments and poly (ε-caprolactone) soft segments. *Polymer* **47**, 4251-4260 (2006).

134 Hu, J. *et al.* Revealing the morphological architecture of a shape memory polyurethane by simulation. *Scientific Reports* **6**, 29180 (2016).

135 Li, Q. *et al.* Advancing reversible shape memory by tuning the polymer network architecture. *Macromolecules* **49**, 1383-1391 (2016).

136 Mehrpouya, M. *et al.* 4D printing of shape memory polylactic acid (PLA). *Polymer* **230**, 124080 (2021).

137 Kotikian, A. *et al.* Innervated, self-sensing liquid crystal elastomer actuators with closed loop control. *Advanced Materials* **33**, 2101814 (2021).

138 Li, S. *et al.* Digital light processing of liquid crystal elastomers for self-sensing artificial muscles. *Science Advances* **7**, eabg3677 (2021).

139 Stepulane, A., Ahlgren, K., Rodriguez-Palomo, A., Rajasekharan, A. K. & Andersson, M. Lyotropic liquid crystal elastomers for drug delivery. *Colloids and Surfaces B: Biointerfaces* **226**, 113304 (2023).

140 Hussain, M. *et al.* Liquid crystal elastomers for biological applications. *Nanomaterials* **11**, 813 (2021).

141 Javed, M., Tasmim, S., Abdelrahman, M. K., Ambulo, C. P. & Ware, T. H. Degradation-induced actuation in oxidation-responsive liquid crystal elastomers. *Crystals* **10**, 420 (2020).

142 Ohm, C., Haberkorn, N., Theato, P. & Zentel, R. Template-based fabrication of nanometer-scaled actuators from liquid-crystalline elastomers. *Small* **7** (2011).

143 Boothby, J. M., Kim, H. & Ware, T. H. Shape changes in chemoresponsive liquid crystal elastomers. *Sensors and Actuators B: Chemical* **240**, 511-518 (2017).

144 Agrawal, A., Yun, T., Pesek, S. L., Chapman, W. G. & Verduzco, R. Shape-responsive liquid crystal elastomer bilayers. *Soft Matter* **10**, 1411-1415 (2014).

145 Guo, W. *et al.* Aligned carbon nanotube/polymer composite fibers with improved mechanical strength and electrical conductivity. *Journal of Materials Chemistry* **22**, 903-908 (2012).

146 Huang, Q. When polymer chains are highly aligned: a perspective on extensional rheology. *Macromolecules* **55**, 715-727 (2022).

147 Feng, J., Levine, H., Mao, X. & Sander, L. M. Alignment and nonlinear elasticity in biopolymer gels. *Physical Review E* **91**, 042710 (2015).

148 Dobrynin, A. V. & Carrillo, J.-M. Y. Universality in nonlinear elasticity of biological and polymeric networks and gels. *Macromolecules* **44**, 140-146 (2011).

149 Hammad, A. *et al.* Theory of the deformation of aligned polyethylene. *Proceedings of the Royal Society A: Mathematical, Physical and Engineering Sciences* **471**, 20150171 (2015).

150 Wang, Y., Gao, J., Dingemans, T. J. & Madsen, L. A. Molecular alignment and ion transport in rigid rod polyelectrolyte solutions. *Macromolecules* **47**, 2984-2992 (2014).

151 Chanda, A., Sinha, S. K. & Datla, N. V. Electrical conductivity of random and aligned nanocomposites: Theoretical models and experimental validation. *Composites Part A: Applied Science and Manufacturing* **149**, 106543 (2021).

152 Tang, Z. *et al.* Uniaxial stretching-induced alignment of carbon nanotubes in cross-linked elastomer enabled by dynamic cross-link reshuffling. *ACS Macro Letters* **8**, 1575-1581 (2019).

153 Zhang, S. *et al.* Creating polymer hydrogel microfibres with internal alignment via electrical and mechanical stretching. *Biomaterials* **35**, 3243-3251 (2014).

154 Chen, Z.-R. & Kornfield, J. A. Flow-induced alignment of lamellar block copolymer melts. *Polymer* **39**, 4679-4699 (1998).

155 G. Cunha, M. A. & Robbins, M. O. Effect of flow-induced molecular alignment on welding and strength of polymer interfaces. *Macromolecules* **53**, 8417-8427 (2020).

156 Kakade, M. V. *et al.* Electric field induced orientation of polymer chains in macroscopically aligned electrospun polymer nanofibers. *Journal of the American Chemical Society* **129**, 2777-2782 (2007).

157 Feller, M., Chen, W. & Shen, Y. Investigation of surface-induced alignment of liquid-crystal molecules by optical second-harmonic generation. *Physical Review A* **43**, 6778 (1991).

158 Zhang, W., Gomez, E. D. & Milner, S. T. Surface-induced chain alignment of semiflexible polymers. *Macromolecules* **49**, 963-971 (2016).

159 Guan, Y. *et al.* Manipulating crystal orientation of poly (ethylene oxide) by nanopores. *ACS Macro Letters* **2**, 181-184 (2013).

160 De Gennes, P. Possibilites offertes par la reticulation de polymeres en presence d'un cristal liquide. *Physics Letters A* **28**, 725-726 (1969).

161 Jin, B. *et al.* Solvent-assisted 4D programming and reprogramming of liquid crystalline organogels. *Advanced Materials* **34**, 2107855 (2022).

162 Ni, Y., Li, X., Hu, J., Huang, S. & Yu, H. Supramolecular liquid-crystalline polymer organogel: Fabrication, multiresponsiveness, and holographic switching properties. *Chemistry of Materials* **31**, 3388-3394 (2019).

163 Singh, V. *et al.* Novel organogel based lyotropic liquid crystal physical gels for controlled delivery applications. *European Polymer Journal* **68**, 326-337 (2015).

164 Aphonin, O., Panina, Y. V., Pravdin, A. B. & Yakovlev, D. Optical properties of stretched polymer dispersed liquid crystal films. *Liquid Crystals* **15**, 395-407 (1993).

165 Cupelli, D. *et al.* Self-adjusting smart windows based on polymer-dispersed liquid crystals. *Solar Energy Materials and Solar Cells* **93**, 2008-2012 (2009).

166 Jain, S. & Rout, D. Electro-optic response of polymer dispersed liquid-crystal films. *Journal of applied physics* **70**, 6988-6992 (1991).

167 Shaik, S., Gorantla, K., Mishra, S. & Kulkarni, K. S. Thermal and cost assessment of various polymer-dispersed liquid crystal film smart windows for energy efficient buildings. *Construction and Building Materials* **263**, 120155 (2020).

168 Vaz, N. A. Polymer-dispersed liquid crystal films: materials and applications. *Liquid crystal chemistry, physics, and applications* **1080**, 2-10 (1989).

Appendix A. Supporting information for Chapter 2

Light transmission of LC polymers:

The light transmission of unpolarized light through the LC polymers was measured using a Perkin Elmer Lambda 950 UV–visible spectrophotometer. Representative light transmission spectra for homopolymers of LCM1 and LCM3 is shown in Figure 23. The average light transmission of the LC polymers with wavelengths ranging from 450 nm to 550 nm were used in Equation (1) of the main text.

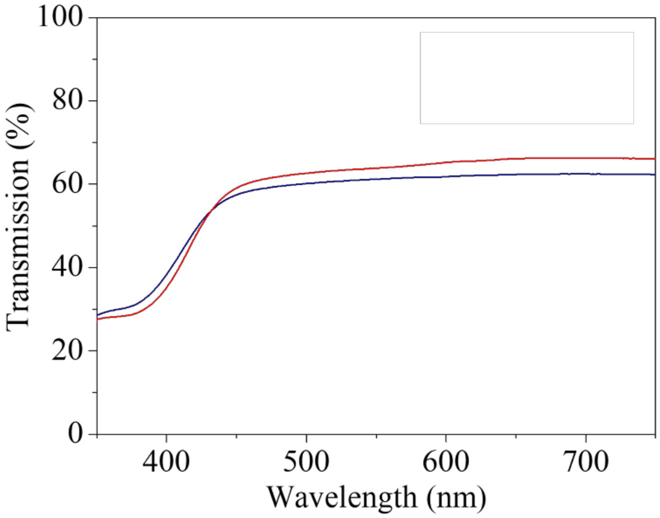

Figure 23. Light transmission spectra for homopolymers of LCM1 (blue) and LCM3 (red). The thickness of the LC polymer samples is ~50 µm.

Effect of crosslinker on $T_{\mathrm{LC-I}}$ of LC polymers

Here we investigate the effect of the non-LC crosslinker, HDDA, on the thermal properties of the LC polymers. In our experiments, we synthesized and characterized LCM1 homopolymers with and without HDDA. Inspection of Figure 24 reveals no significant difference in the $T_{\mathrm{LC–I}}$ values of LCM1 with 0 and 2.5% by weight of HDDA.

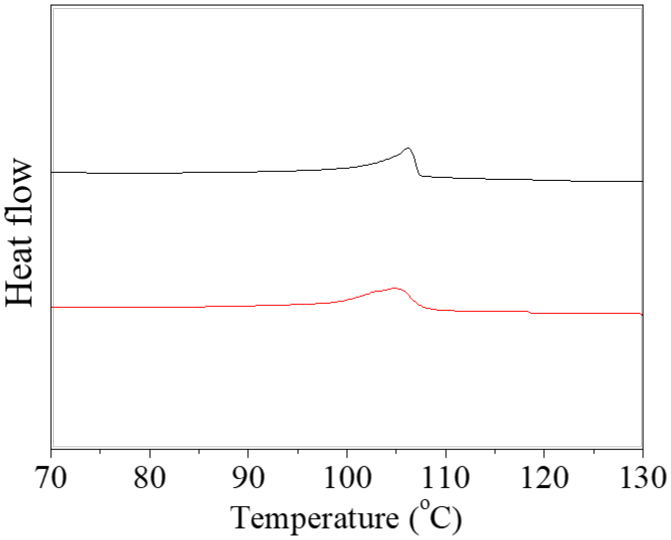

Figure 24. DSC traces of LCM3 homopolymers with (red) and without (black) crosslinker HDDA. The weight fraction of HDDA was 2.5% wt based on the total mass of the homopolymer. Cooling rate: 2 °C/minute.

X-ray scattering of LC polymers

We performed wide angle x-ray scattering (WAXS) to confirm the alignment of the LC director along the z-axis in homopolymers of LCM1 and LCM3. Inspection of Figure 25 reveals that the LC functional groups of the LC homopolymers are aligned parallel with the direction of the applied magnetic field.

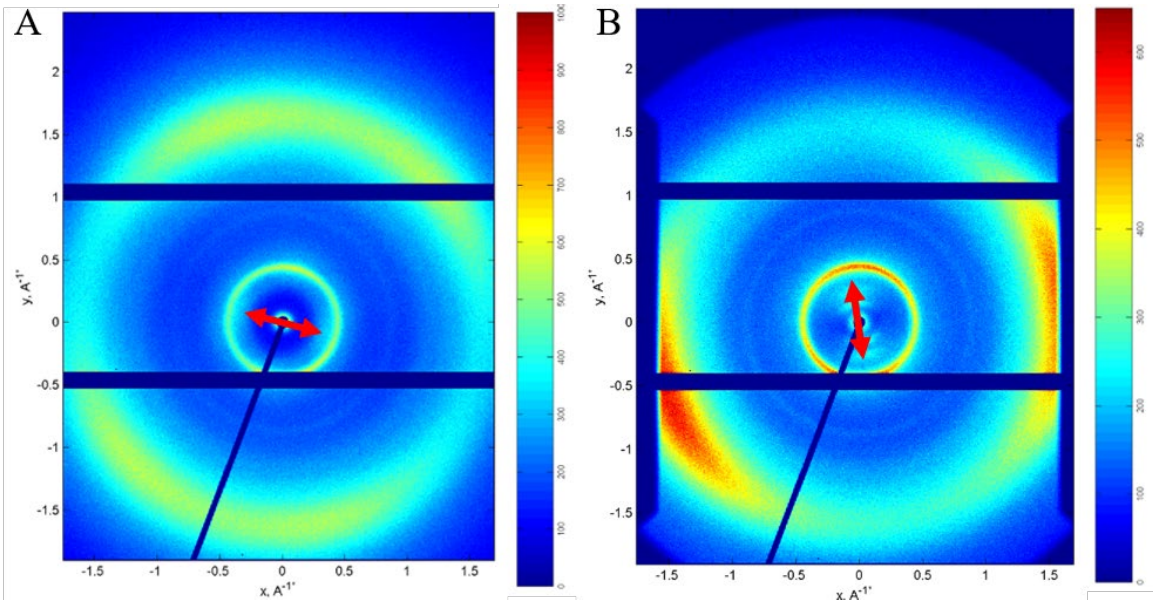

Figure 25. 2D x-ray scattering as a function of azimuthal angle and momentum transfer corresponding to (A) LCM3 and (B) LCM1 homopolymers. Red, double-headed arrows indicate the magnetic field orientation during LC homopolymer synthesis.

To provide further insights into the effect of the random polymer structure, we estimated the scalar order parameter of the LC polymers using x-ray analysis. Specifically, the scalar order parameter can be calculated by:

$$\text{Scalar order parameter} = \frac{1}{2}\left(3\langle \cos^2 \beta \rangle - 1\right) \tag{S1}$$

where β is the angle between a LC molecular symmetry axis and the director of the LC functional groups in LC polymers. $\langle \cos^2 \beta \rangle$ can be calculated by:

$$\langle \cos^2 \beta \rangle = \frac{\sum_{n=0}^{5} \frac{f_{2n}}{2n+3}}{\sum_{n=0}^{5} \frac{f_{2n}}{2n+1}} \tag{S2}$$

$$I(\theta) = f_0 + \frac{2}{3} f_2 \cos^2\theta + \frac{8}{15} f_4 \cos^4\theta + \frac{16}{35} f_6 \cos^6\theta + \frac{128}{315} f_8 \cos^8\theta + \frac{256}{693} f_{10} \cos^{10}\theta \tag{S3}$$

in which I and θ are the scattering intensity and angle, respectively. We estimated the scalar order parameter of the homopolymers of LCM1 and LCM3 and the random copolymer of LCM1–LCM2 and LCM1–LCM3 to be ~ 0.250, ~ 0.275, ~ 0.278 and ~ 0.102, respectively. The LCM1 composition of the random copolymers is 40% by weight.

NMR characterization of LC polymers

Here we performed NMR characterization to confirm the full conversion of the LC monomers during photopolymerization. The LC polymers were dissolved in deuterated chloroform, and the NMR measurement was conducted on a 400 MHz Advance NEO ^{1}H NMR. As evidenced in Figure 26, the disappearance of the peaks between 5.5–6.5 ppm in the ^{1}H NMR measurements, which corresponds to the non-aromatic C=C double bonds, indicates a full conversion of the reactive LC monomers during photopolymerization. In addition, the weak peaks around 7.5–8.0 ppm can be attributed to the aromatic ring in 2-hydroxy-2-methylpropiophenone, which is the remaining photoinitiator.

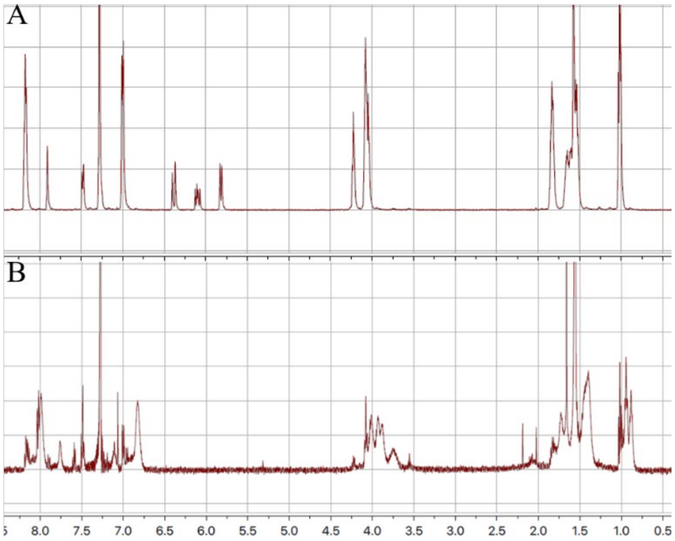

Figure 26. ^{1}H NMR spectrum of LCM1 monomer (A) before and (B) after polymerization.

Molecular weight and polydispersity of LC (co)polymers

Here we performed GPC measurements to characterize the number-average molecular weight (M_n), weight-average molecular weight (M_w), and PDI (M_w/M_n) of the LC (co)polymers synthesized in this work. The measurement results are summarized in Table 1.

Table 1. Molecular weight and polydispersity of LC (co)polymers.

Composition LCM1 (wt%)	*Composition LCM2 (wt%)*	*Composition LCM3 (wt%)*	Mn (g/mol)	Mw (g/mol)	PDI
100	*0*	*0*	20023	31550	1.58
0	*100*	*0*	26268	45413	1.73
0	*0*	*100*	25732	48751	1.89
80	*20*	*0*	20510	34574	1.69
60	*40*	*0*	20896	37628	1.80
40	*60*	*0*	23730	54282	2.29
20	*80*	*0*	20042	30464	1.52
80	*0*	*20*	20637	33047	1.60
60	*0*	*40*	18709	31301	1.67
40	*0*	*60*	19601	36342	1.85
20	*0*	*80*	22278	53952	2.42
0	*80*	*20*	21487	35303	1.64
0	*60*	*40*	17822	38105	2.14
0	*40*	*60*	19357	34642	1.79
0	*20*	*80*	23130	50911	2.20

DSC measurement of random LC copolymers

Here we performed DSC characterization to determine the T_{LC-I} of the random LC copolymers. As evidenced in Figure 27, the T_{LC-I}s of the LCM1–LCM2 random copolymers lie between the T_{LC-I}s of the respective homopolymers, whereas the T_{LC-I}s of the LCM1–LCM3 random copolymers lie below the T_{LC-I}s of the respective homopolymers.

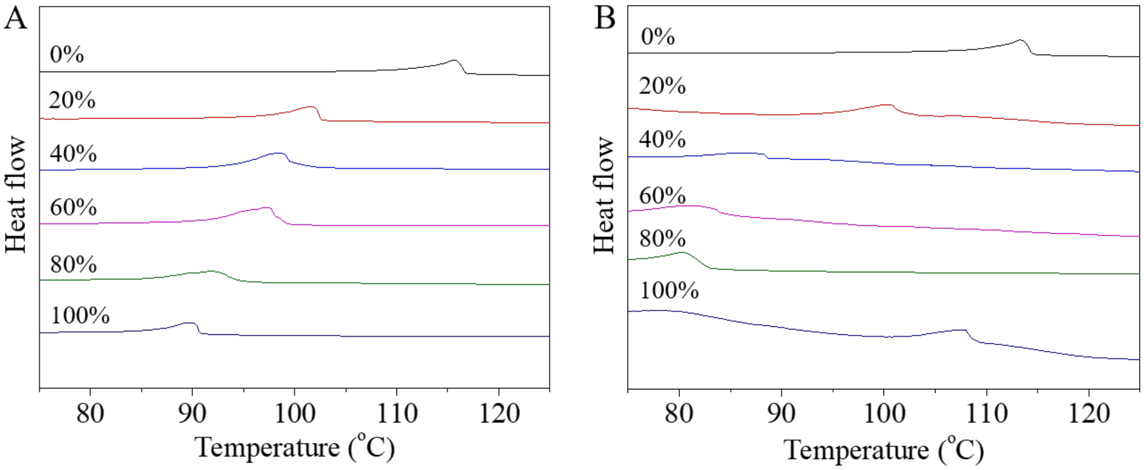

Figure 27. Representative DSC traces for random copolymers of (A) LCM1–LCM2 and (B) LCM1–LCM3 as a function of chemical composition. The percentage indicates the composition of (A) LCM2 and (B) LCM3 in the LC copolymers. Cooling rate: 2 °C/minute.

DSC measurement of LC homopolymer mixtures

To provide insights into the LC monomer configuration-dependent T_{LC-I} of the random LC copolymers, we measured the thermal properties of mixtures of LC homopolymers. In contrast to the random LC copolymers which exhibit a single T_{LC-I}, the homopolymer mixture shows two individual T_{LC-I}s corresponding to each homopolymer, as shown in

Figure 28. We hypothesize that the existence of two $T_{LC–I}$s is due to incomplete mixing of two different LC homopolymers.

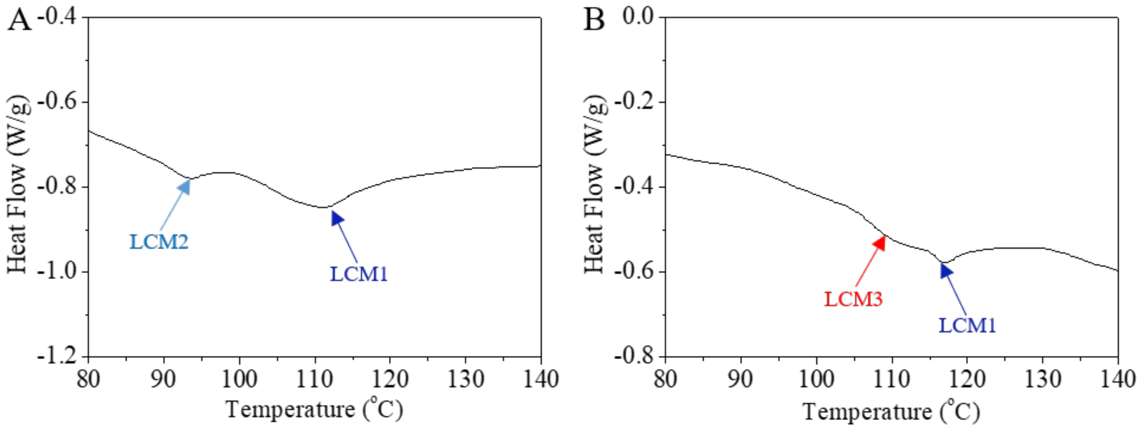

Figure 28. DSC traces of homopolymer mixtures of (A) LCM1–LCM2 and (B) LCM1–LCM3. The weight fraction of LCM1 homopolymers is 60% by weight based on the total mass of the homopolymer mixture. Heating rate: 2 °C/minute.

Thermal behavior of LCM2-LCM3 random copolymer

Here we characterized the thermal properties of the other pair of random copolymers consisting of different configurations of LC monomers (e.g., LCM2 and LCM3). As shown in Figure 29A, the $T_{LC–I}$s of the LCM2–LCM3 random copolymers lie below the $T_{LC–I}$s of the respective homopolymers (90 °C and 107 °C for LCM2 and LCM3 homopolymers, respectively). In addition, Figure 29B shows that the $T_{LC–I}$s of the unpolymerized mixtures lie between the $T_{LC–I}$s of the respective monomers. The characteristic behaviors of the LCM2–LCM3 random copolymer is similar to the LCM1–LCM3 random copolymer.

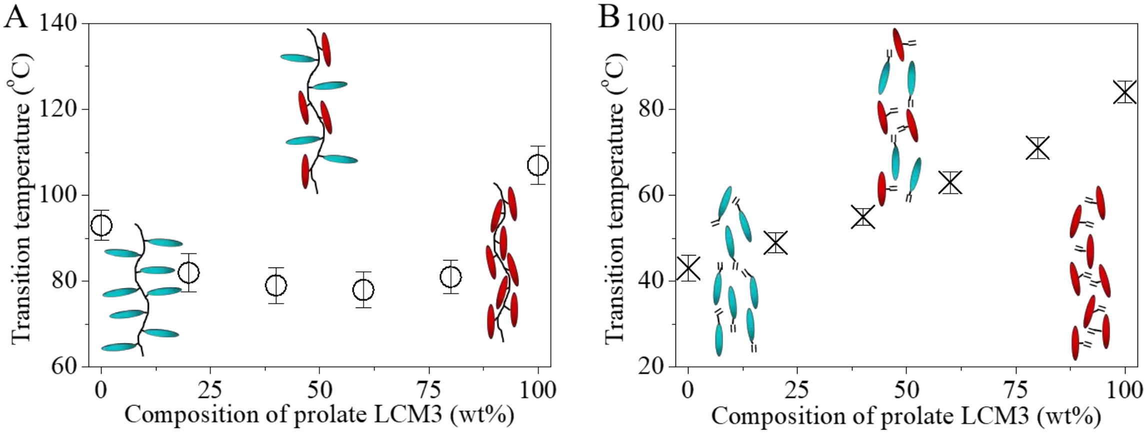

Figure 29. $T_{LC–I}$s of (A) random copolymers and (B) unpolymerized mixtures consisting of different configurations of LC monomers (LCM2–LCM3) as a function of monomer composition.

$T_{LC\text{-}I}$s of LC polymers synthesized by RAFT polymerization

To provide further insights into the origin of the LC monomer configuration-dependent $T_{LC–I}$s of the LC copolymers, we used RAFT solution polymerization to synthesize statistically random LC copolymers. As shown in Figure 30, no measurable difference in the $T_{LC–I}$ was observed between LC copolymers synthesized with and without RAFT agents. These results show that the influence of reactivity ratios of different LC monomers on the composition-dependent $T_{LC–I}$s of the random LC copolymers is negligible.

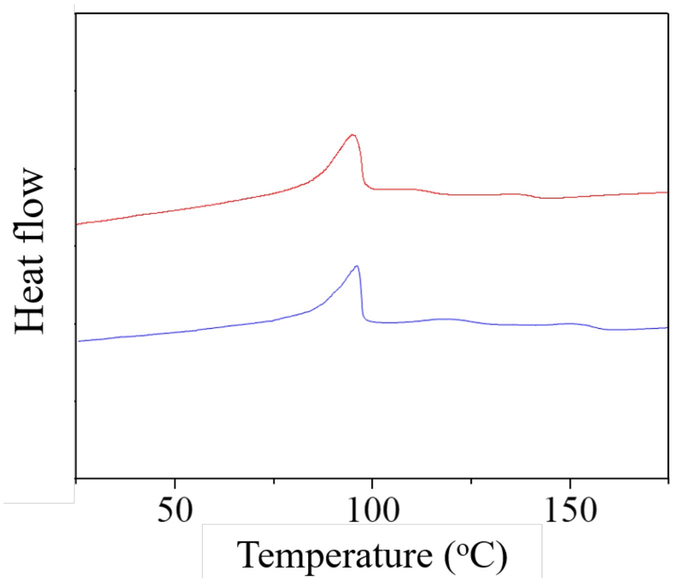

Figure 30. $T_{LC\text{–}I}$s of LCM1–LCM3 random copolymers synthesized with (red) and without (blue) RAFT agent. The composition of LCM1 is 60% by weight based on the total mass of the random copolymer. [RAFT]:[DMPAP]:[LC monomer] = 1:1:100. Cooling rate: 2 °C/minute.

Appendix B. Supporting information for Chapter 3

Investigation of the effect of film thickness on the maximum curvature of LCE films

Here we investigated the maximum curvature of nanowire augmented liquid crystal elastomer (LCE) films with different thickness. To create the films with different thicknesses, spacers with different thicknesses were used to create the optical cells. As can be seen in Figure 31, the thickness of the films has a drastic effect on the maximum curvature of the films, with thin samples curling more than thicker films. For a majority of the results, a thickness of 0.5 was used.

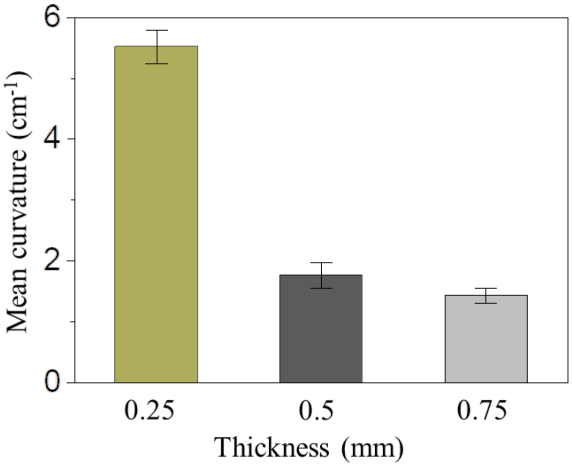

Figure 31. Effect of thickness on the maximum curvature of the nanowire-augmented LCE films.

Investigation of the effect of nanowires on the maximum curvature of LCE films

Here we investigated whether the nanowires had any effect on the maximum curvature of the nanowire augmented LCE films. The same films were used for both tests, with the nanowires being carefully removed with a scalpel to avoid damaging the bulk of the film. The removal of the nanowires was confirmed visually, by a shiny appearance matching the backside of the film. As can be seen in Figure 32, the nanowires were found to not have a significant effect on the maximum curvature of the film. Therefore, we can assume that the nanowires are not causing or hindering the curling motion.

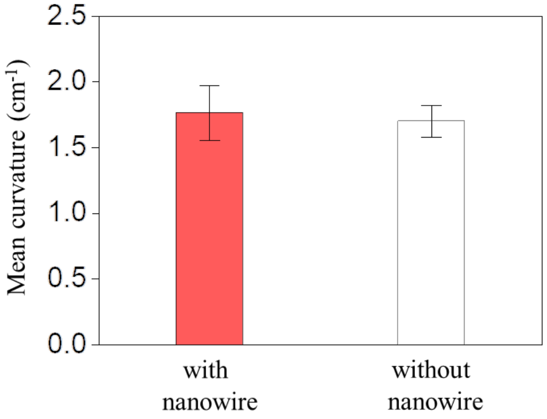

Figure 32. Effect of nanowires on the maximum curvature of the LCE films.

Appendix C. Supporting information for Chapter 4

Polarized optical micrographs of PDLCs and LCgels

Figure 33 shows polarized optical micrographs of polymer dispersed liquid crystal (PDLC) films (Figure 33C) and liquid crystal gels (Figure 33B) after the removal of the liquid crystal. As can be seen compared to the aligned film made through ASAP (Figure 33A), the two films are dark at all angles of rotation.

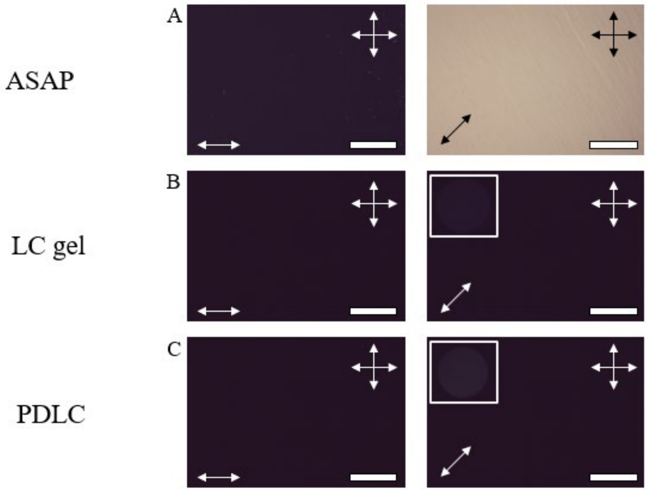

Figure 33. Polarized optical micrographs of ASAP films, LC gels, and PDLCs after LC removal. Scale bars, 200 μm.

Confirming the removal of E7

Figure 34 shows attenuated total reflectance-Fourier transform infrared (ATR-FTIR) spectroscopy data of a film prepared through ASAP before and after LC removal. As can be seen by the disappearance of the peak at 2224 cm^{-1}, corresponding to the CN group of the E7, the LC can be assumed to be completely removed from the films after washing in ethanol.

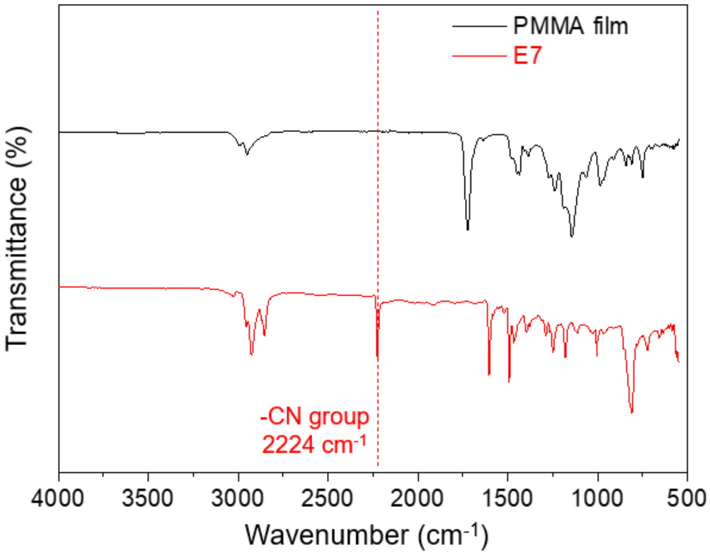

Figure 34. ATR-FTIR spectra confirming removal of E7 from PMMA film.